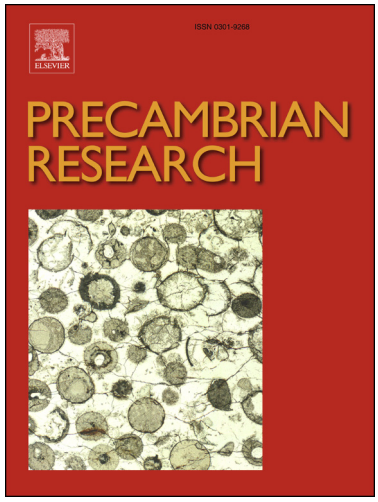

Neoarchean microblock amalgamation in southern India: evidence from the Nallamalai Suture Zone

Shan-Shan Li, M. Santosh, Sohini Ganguly, P.V. Thanooja, K. Sajeev, Arijit Pahari, C. Manikyamba

PII: S0301-9268(18)30127-X
DOI: https://doi.org/10.1016/j.precamres.2018.05.017
Reference: PRECAM 5089

To appear in: *Precambrian Research*

Received Date: 4 March 2018
Revised Date: 12 May 2018
Accepted Date: 15 May 2018

Please cite this article as: S-S. Li, M. Santosh, S. Ganguly, P.V. Thanooja, K. Sajeev, A. Pahari, C. Manikyamba, Neoarchean microblock amalgamation in southern India: evidence from the Nallamalai Suture Zone, *Precambrian Research* (2018), doi: https://doi.org/10.1016/j.precamres.2018.05.017

Neoarchean microblock amalgamation in southern India: evidence from the Nallamalai Suture Zone

Shan-Shan Li[1*], M. Santosh[1,2], Sohini Ganguly[3], P.V. Thanooja[4], K. Sajeev[4], Arijit Pahari[5], C. Manikyamba[5]

[1]*School of Earth Sciences and Resources, China University of Geosciences Beijing, 29 Xueyuan Road, Beijing 100083, China;*

[2]*Centre for Tectonics, Exploration and Research, University of Adelaide, Adelaide SA 5005, Australia;*

[3]*Department of Earth Science, Goa University, Taleigao Plateau, Goa-403206, India*

[4]*Centre for Earth Sciences, Indian Institute of Science, Bangalore 560012, India*

[5]*National Geophysical Research Institute (Council of Scientific and Industrial Research), Uppal Road, Hyderabad 500007, India*

Corresponding author E-mail: lishanshan@cugb.edu.cn

Abstract

A collage of crustal blocks ranging in age from Mesoarchean to Neoarchean accreted to the southern margin of the Dharwar Craton in Peninsular India preserve distinct evolutionary history, but share a common metamorphic record during Archean-Proterozoic transition. Here we investigate the tectonic boundary between two of these microblocks, the Shevaroy Block to the west and the Madras Block to east, termed as the Nallamalai Suture Zone (NLSZ). We present integrated field, petrological, geochemical and zircon U-Pb and Lu-Hf data from a suite of meta-igneous and metasedimentary units along the NLSZ and its flanks. Zircon grains from the meta-monzogranite, hornblende-biotite gneiss, amphibolite, granodiorite, diorite, charnockite, BIF (banded iron formation) and BMQ from this area show magmatic emplacement ages clustering around 2.50 to 2.56 Ga, except for the meta-monzogranite showing ages up to 3.2 Ga, correlating with long-lived convergent margin magmatism through multiple slab melting episodes. All the rocks show tightly constrained early Paleoproterozoic (ca. 2.46 to 2.48 Ga) metamorphic ages, including the metamorphic zircon in the BIFs, marking the timing of collision of the two continental blocks with consumption of the intervening oceanic lithosphere. The εHf(t) values of magmatic zircon grains from the different rock types range from -4.1 to +5.7, and together with T_{DM}^{C} Hf model ages of 2672-3247 Ma, a dominantly juvenile crust growth is indicated, which initiated around 3.3 Ga and continued to 2.7 Ga, followed by crustal reworking in a continental arc

towards the end of Neoarchean.

The geochemical data suggest that tholeiitic to calc-alkaline parental melts for the mafic-intermediate-felsic suite were generated by low degree partial melting of a peridotitic mantle wedge metasomatized by subduction-derived fluids and sediments and continuous slab melting ensued by intracrustal fractional crystallization of melts with reworking of older continental crust. The BIF and BMQ samples display positive Eu anomalies, negative to negligible Ce anomalies, and superchondritic Y/Ho ratios suggesting their formation in an oceanic realm proximal to an active continental margin setting. The magmatic and tectonic attributes are consistent with eastward oceanic subduction and ocean closure along the NLSZ which is defined here as the trace of a suture welding the Shevaroy and Madras Blocks. We envisage that multiple subduction and amalgamation of several microblocks occurred in the Dharwar Craton and its southern domains, amalgamating several microblocks during the Archean – Paleoproterozoic transition.

Keywords: Crustal evolution; microblock amalgamation; Zircon geochronology and Lu-Hf isotopes; Geochemistry; Nallamalai Suture Zone

1. Introduction

Cyclic episodes of amalgamation and dispersal of continental blocks and peripheral accretions have played pivotal roles in the evolution of the Earth's crust (Nance et al., 2014, Cawood et al., 2016). Although top-down processes related to lithospheric plate interactions and mantle plume influenced bottom provide key geodynamic drivers for continental dynamics (Cawood et al., 2016), the major geological process contributing to crustal growth is arc magmatism, and continental crust may is sometimes even be destroyed during collisional orogenesis (Clift et al., 2009; Roberts et al., 2015) Suture zones preserved with the continents mark the sites of continental collision and terrane accretion and also record multiple magmatic and metamorphic events (Li et al., 2016; Loose and Schenk, 2018). Terrane accretions and continental collisions are envisaged to be principal contributors to the growth of continental crust (Dhuime et al., 2012). The allochthonous, exotic geologic units that originated through sinking of oceanic lithosphere were transferred to the overriding plate by accretionary processes during subduction. These include island arcs, oceanic plateaus, submarine ridges, seamounts,

continental fragments (Tetreault and Buiter, 2014). Suture zones preserved with continents mark sites of earlier ocean-ocean or ocean-continent convergence and subduction and bear the signatures of magmatic and metamorphic events associated with the terrane accretion, continental collisional and exhumation processes (Touret et al, 2016). The rapid continental growth in Archean reaching a peak at ~2.7 Ga was followed by a steady state growth, with two distinct tectonic modes are recognized for continental growth (Touret et al, 2016). Lateral growth of continents occurs above oceanic subduction zones by top-down magmatic processes in a high pressure metamorphic regime, whereas vertical growth of continents invoke accumulation of mantle derived magmas at the base of the crust by bottom up process in a high temperature metamorphic regime (Touret et al., 2016).

Southern Peninsular India preserves the geological records of multiple crust formation, recycling and destruction from Eoarchean to Cambrian (Collins et al., 2014; Santosh et al., 2009, 2015). The Dharwar Craton and surrounding Archean crustal blocks provide a window to study Precambrian continent building through terrane accretion and involving multiple subduction-collision processes (Chardon et al., 2011; Kumar et al., 2013; Jayananda et al., 2014; Manikyamba et al., 2017; Santosh and Li, 2018). Among these, one of the little known region is the zone between the Shevaroy and Madras Block surrounding the southern part of the Eastern Dharwar Craton, and marked by

a prominent divide termed as the Nallamalai Suture Zone (Fig. 1), identified as one of the major high strain zones in southern India (Drury et al., 1984). In this study, we investigate this zone and the flanks of the crustal blocks on either side in terms of detailed field studies, petrology, geochemistry and zircon U-Pb and Lu-Hf isotopes. Our results provide important insights into the nature and timing of magmatic episodes and metamorphism associated with the amalgamation of two microblocks and destruction of the intervening ocean floor with the Nallamalai Suture Zone representing the trace of an oceanic suture. Our study has important implications on crustal evolution in southern India during Archean-Paleoproterozoic transition.

2. Geological background and sampling

2.1 Geological background

The Dharwar Craton which forms of the Archean nuclei in Peninsular India has been generally divided into the Western Dharwar Craton (WDC) and Eastern Dharwar Craton (EDC) (Chadwick et al., 2000; Jayananda et al., 2000, 2013; Lancaster et al., 2015; Rao et al., 2015) (Fig. 1). Among these, the WDC preserves the oldest nucleus with ages in the range of 3.4-3.0 Ga and is dominantly composed of Archean greenstone belts, felsic orthogneiss, TTG, amphibolite, intruded by 2.5 Ga granitoids (Chadwick et al., 2000; Maibam et al., 2016; Manikyamba et al., 2017). The Archean greenstones of the WDC were subdivided into the >3.2 Ga Sargur Group and the 2.9-2.55 Ga

Dharwar Supergroup (Chadwick et al., 2000; Jayananda et al., 2014). In the northwestern part of the WDC, the Kumta Suture separates the Karwar region which is considered as a microblock, where the TTG gneiss shows the magmatic emplacement age of ca.3.2 Ga (Kumar et al., 2013). The EDC is composed of Late Archean to Early Proterozoic (2.7-2.5 Ga) felsic orthogneiss, granites and charnockite (Maibam et al., 2016; Santosh et al., 2003). Some of the recent studies demarcated the Central Dharwar Craton (CDC) as a discrete unit between the WDC and EDC, marked by the Chitradurga greenstone belt, and felsic orthogneisses, together with the ca. 400 km long and 20-30 km wide Closepet granitoid batholith (Moyen et al., 2003, 2001; Chardon et al., 2011). The Chitradurga greenstone belt is composed of 2.7-2.5 Ga metabasalts, BIFs, amphibolite and metagabbros (Chardon et al., 2011). The magmatic emplacement events in the CDC are constrained as 3.2-2.9 Ga for the basement and 2.6-2.5 Ga for the granite and greenstones (Chardon et al., 2011; Santosh and Li, 2018). The northwestern part of the Dharwar Craton is covered by the Cretaceous-Tertiary Deccan Volcanics.

To the south of Dharwar Craton are several crustal blocks including Coorg, Biligiri Rangan, Shevaroy (including Salem) and Madras (Santosh et al., 2015; Kumar et al., 2016; Peucat et al., 2013; Glorie et al., 2014). The Coorg Block is located along the southern margin of the WDC, the core of which comprises >3.3 Ga to 3.1 Ga charnockites, TTG gneisses and

granitoids, in the absence of the 2.5 Ga thermal event and hence considered as an exotic block (Santosh et al., 2015). The NW-SE trending Mercara Suture Zone in the east and the Moyar Suture Zone in the south separate the Coorg Block to the west (Yano et al., 2016; Santosh et al., 2015). The ultramafic, mafic and felsic suite including charnockites from the Wynad region along the junction of the Mercara and Moyar Suture Zones show magmatic ages in the range of 3.3-2.5 Ga, with minor zircons from the metadiorite and metagabbro formed at 2.5 Ga (Yang et al., 2016; Yano et al., 2016). To the south of EDC, the Mettur Suture Zone separates the Biligiri Rangan Block to the west and Salem/Shevaroy Block to the east. The Biligiri Rangan Block is mainly composed of charnockite at is core, surrounded by felsic orthogneiss and granitoids in the northern part of the block. Two stages of magmatic events are recorded at 3.3-3.1 Ga, and at 2.5 Ga (Peucat et al., 2013; Kumar et al., 2016). The Shevaroy Block is composed of the Krishnagiri area and part of the Salem Block (previous classification) and is dominantly composed of charnockites and felsic orthogneisses. Age data on the charnockite, migmatite and granite gneiss from the Shevaroy Block show magma emplacement at ca.2.76-2.53 Ga (Peucat et al., 2013; Glorie et al., 2014; Clark et al., 2009). The Nallamalai Suture Zone separates the Shevaroy and Madras Blocks. The Madras Block is dominantly composed of charnockite, migmatite, granite and felsic orthogneiss, and although there are only few reports on age data from this block, the available information on

charnockite and granodiorite show emplacement during 2.58-2.53 Ga (Crawford, 1969; Bernard-Griffiths et al., 1987).

Our study area broadly traverses the NW-SE trending Nallamalai Suture Zone and its flanks with Shevaroy Block to the west and Madras Block to the east (Fig. 2). The region is dominantly composed of charnockite, amphibolite, mafic granulite, hornblende biotite gneiss and metapelitic rocks. The area comprises Khondalite Group, Charnockite Group, Ultramafic Complex, Migmatite Complex, Sargur Group, Peninsular Gneissic Complex, Kolar Group, Alkali and Ultramafic Complex and Khondalite Group according to the classification of the Geological Survey of India (1987). The khondalite group includes garnet-sillimanite gneiss and quartzite, and the charnockite group comprises charnockite, pyroxene granulite and magnetite quartzite. The pyroxene granulites occurs as NE-SW trending linear bands associated with charnockites. Hornblende-biotite gneiss and granite constitute the Migmatite Complex. The Sargur Group includes fuchsite quartzite, cordierite-sillimanite-mica schist and amphibolite. The Kolar Group comprise schistose amphibolite, banded ferruginous quartzite (BFQ), gneiss and metabasalt. Several granitoid intrusions and younger alkaline ultramafic intrusions and dolerite dykes also occur in the area (Geological Survey of India, 1987).

We carried out systematic field investigations and sampling of the various

representative rock types from the eastern margin of the Shevaroy Block, within the Nallamalai Suture Zone and the western margin of the Madras Block to cover the suture and collision belt. Our samples include charnockites (both garnet-bearing and garnet-absent), granodiorite, granite, meta-monzogranite, Grt-Bt gneiss, granitic pegmatite, diorite, amphibolite, BIF and BMQ. The sample locations are shown in Figure 2.

2.2. Geology of the study area and sampling

The location, co-ordinates and salient details of the nineteen representative samples from various rocks types used in this study are given in Table 1. A brief description of their field setting is given below.

Granitoids

The meta-monzogranite (NM-8-1) collected from a ground level exposure along the road from Tirupathur to Matrapalli village is a well-foliated hornblende gneiss (Fig. 3F). The rock is medium to coarse grained and profusely traversed by millimeter sized veins of pink granite. Near Singapalayam village (NM-12-1), a wide well cutting made for irrigation purposes expose the basement rock composed of Hbl gneiss. The Hbl gneiss is coarse grained and contains disrupted layers (~10cm) of fine grained greenish hornblendite. The granodiorite (NM-3-1) was collected from a large

rocky hill on the western side of the road to the north Karimarigalam. The rock is medium grained and well-foliated defined with biotite- and hornblende-rich layers with minor greenish clinopyroxene (Fig. 3B). The granodioritic gneiss is variably migmatised with light pink veins and pools of granitic material defining compositional layering. On the way to Pochampalli, near Appukottai village, foliated metagranite (NM-4-1) is exposed. The rock is medium to coarse grained with pink K-feldspar (Fig. 3C). The metagranite carries varying sized stretched enclaves and schlierens of dioritic material which lack any obvious foliation.

The charnockite sample NM-2-1 was collected from a chain of working quarries exposing few hundred meters width of greyish green medium to coarse grained, sporadically veined by pink migmatitic granite (Fig. 3A). The charnockite is generally massive with weak foliation defined by biotite. Another garnet-bearing charnockite (sample NM-11-1) comes from roadside outcrops in Govindapuram village with coarse grained garnet and orthopyroxene. The rock shows prominent compositional banding and foliation defined by biotite, garnet and felsic minerals (Fig. 4A). The basement rocks in the surrounding regions are all charnockite. On the way from Tirupathur to Thiruvannarralai, large hillocks from Singarapettai to Ananthavadi expose massive charnockites. The charnockite (NM-13-1) is typically grayish green, medium grained and weak foliated, with clots and bands of orthopyroxene-rich

domains with very little biotite and without garnet. Another garnet-bearing charnockite (NM-16-2) was collected from a roadside exposure near Melvanakkarnloadi with medium grained garnet, scattered orthopyroxene and sporadic biotite (Fig. 4F). The rocks shows distinct compositional banding and weak gneissosity.

Granitic pegmatite

Pegmatite sample (NM-16-1) was collected from the same location where the charnockites are exposed (sample NM-16-2). The pegmatite is deformed and fragmented with coarse and massive fractured quartz together with K-feldspar and minor plagioclase.

Diorite

Diorite sample NM-2-2 was collected from a 0.5m wide enclave within charnockite (NM-2-1). The rock is medium to fine grained and melanocratic. Several dioritic enclaves of varying size occur within the charnockite similar to magma mixing and mingling structure.

Grt-Bt gneiss

Near Naradapattu village, thick bedded sequence of hornblende gneiss with

sporadic garnet and carrying bands and boudins of fine grained pyroxene gneissic rock (NM-17-1) is exposed in a large quarry. In the eastern part of the quarry, the migmatized hornblende gneiss is intruded by pink granite. Medium to coarse grained and foliated Grt-Bt gneiss with abundant garnet and minor biotite occur as disrupted dykes and boudins within the hornblende gneisses.

Amphibolite

In the Piranjunur area, south east of Pochamapalli, migmatitic amphibolite and hornblende gneiss (NM-5-1, NM-5-2, NM-5-3) are exposed in a large sub-surface quarry, ~80-100m in length and ~10m height. The rock is veined by pink granite (Fig. 3D, 3E). Fine grained greenish amphibolite occurs as few meter-sized blocks or small enclaves and bands within the coarse grained hornblende gneiss. Some domains are highly sheared and mylonitised with schistose structure and coarse platy chlorite and greenish clots of epidote. The amphibolite and hornblende gneiss are foliated, whereas the pink granite lacks any visible foliation. Another greenish and well-foliated amphibolite (NM-8-2) was collected from the same location of the meta-monzogranite (NM-8-1) where the rock occurs as boudins within the hornblende gneiss.

Banded Iron Formations and Banded Magnetite Quartzite

Several surface exposures and hillock cuttings near Arasankanni, exposure disrupted fragments of banded iron formation (BIF) (NM-14-1, NM-14-2). The BIF is metamorphosed and contains millimeter-sized alternating layers of iron bearing mineral (brownish hematite/magnetite) with cryptocrystalline quartz (Fig. 4B, C). The layers show mesoscopic folding with broad open to isoclinal folded bands. In the same location, within a well-cutting, fine grained, fresh and dark greenish colored BMQ (banded magnetite quartzite) is exposed (NM-14-3, NM-14-4) (Fig. 4E). The BMQ displays thin millimeter scale layering. In Thandampattu village, a road cutting exposes another large BIF band (NM-15-1) up to 50 m (Fig. 4D). The rock is thinly banded and fractured with laminae of Fe-, and Si-rich domains. The weathered surface shows cherry brown color with hematite. Freshly broken surface shows fine grained dark magnetite. In some domain, the magnetite occurs as recrystallized thick layers of more than 10 cm in width. Pink and green jasper layers are also associated with the rock, suggesting submarine hydrothermal precipitation. .

3. Analytical techniques

A detailed description of the analytical techniques employed in this study relating to petrography, whole rock geochemistry, and zircon U-Pb and Lu-Hf

isotopic analyses are given in Appendix A (supplementary data).

4. Petrology

Meta-monzogranite and Hbl gneiss (NM-8-1, NM-12-1)

The rocks are dominantly composed of K-feldspar (35-38%), plagioclase (25%), quartz (20-25%), hornblende (10%), and minor biotite (2%). The gneissic fabric is defined by alternating quartz and plagioclase layers with hornblende and biotite bearing layers. K-feldspar is medium to coarse grained (0.3 mm) and subhedral. Plagioclase occurs as elongated tabular crystals and is fine to medium grained (>0.2 mm), subhedral to anhedral. Most of the plagioclase grains are partly sericitized. Quartz also occurs as elongated grains. Hornblende is medium to coarse grained (0.2 mm) and some grains are altered to biotite and chlorite.

Grt-Bt gneiss (NM-17-1)

The sample is composed of plagioclase (20%), K-feldspar (22%), quartz (20%), garnet (18%), clinopyroxene (8%), biotite (8%), and magnetite (4%), with accessory zircon (Fig. 5l). Garnet is fine to medium grained (0.25 mm), euhedral to anhedral, with inclusions of biotite and magnetite. Plagioclase is medium grained (0.2 mm), with some grains show strong sericitization. Clinopyroxene is medium to fine grained and angular with brownish color. The sample show weak foliation. Brownish biotite is fine grained, and subhedral to

anhedral.

Granodiorite (NM-3-1)

Sample NM-3-1 is mainly composed of plagioclase (35 %), K-feldspar (25 %), quartz (25%), biotite (8 %), hornblende (5%), and minor clinopyroxene (2%), together with accessory zircon and apatite (Fig. 5C). K-feldspar is medium to coarse grained (0.3 mm) and subhedral to anhedral. Plagioclase is medium grained (<0.3 mm) and subhedral to anhedral. Quartz is fine to medium grained (0.2 mm) and angular. Quartz also occurs in association with feldspar in myrmekite texture. Hornblende is fine to medium grained (0.1 mm) subhedral laths to anhedral with pale greenish color. Biotite is fine to medium grained (<0.1 mm) and sometimes intergrown with hornblende. Some of the hornblende grains are altered into biotite and an aggregate of secondary carbonate minerals. Magnetite is fine to medium grained and angular. Abundant apatite occurs as inclusions in biotite or K-feldspar.

Granite (NM-4-1)

The pink granite is composed of K-feldspar (40 %), plagioclase (28%), quartz (25%), biotite (5%), and magnetite (2%) with accessory zircon and apatite (Fig. 5D). K-feldspar is fine to coarse grained (up to 0.4 mm), euhedral to subhedral, and dominantly perthitic (15%). Some biotite laths are included in K-feldspar. Plagioclase is fine to medium grained (0.1 mm), euhedral to

subhedral. Quartz is medium to coarse grained (0.4 mm) and angular. Magnetite is fine grained and angular. Biotite is brownish and fine grained.

Charnockite (NM-2-1, NM-13-1)

The charnockites are composed of K-feldspar (30%), quartz (25-30%), plagioclase (15-22%), orthopyroxene (8%), and biotite (5-10%), with accessory titanite ,apatite and zircon (Figs. 5A, 5F). Sample NM-2-1 contains minor garnet, clinopyroxene and magnetite. K-feldspar is medium to coarse grained (0.2 to 0.4 mm), subhedral to anhedral, and shows perthitic texture with biotite inclusions. Plagioclase is medium grained (0.25 mm) and euhedral to subhedral with polysynthetic twinning. Some plagioclase grains show sericitization. Quartz is medium to coarse grained (0.2 to 0.3 mm), subhedral to anhedral and shows wavy extinction. Orthopyroxene is medium grained and altered with inclusions of quartz and biotite. Biotite is medium to fine grained (0.2 to 0.1 mm) subhedral to anhedral, and shows dark brownish to greenish pleochroism. Apatite occurs as inclusions in plagioclase or biotites and shows high relief. Magnetite is medium to fine grained and angular.

Garnet-bearing-charnockite (NM-11-1, NM-16-2)

The rocks show a mineral assemblage of K-feldspar (25-30%), quartz (15-20%), plagioclase (15%), garnet (10-12%), orthopyroxene (5-10%), clinopyroxene (5%), biotite (3-5%), and magnetite (3%), with accessory zircon,

titanite and apatite (Fig. 5E, 5H). K-feldspar is medium grained (0.15 to 0.2 mm), subhedral to anhedral. Quartz is medium to fine grained (0.1 mm) with irregular grain boundaries. Plagioclase is medium grained (01. to 0.15 mm), subhedral to anhedral, and some grains show partial sericitization. Garnet is pale pink colored and fine to medium grained (0.1 to 0.15 mm), and contains plagioclase and biotite inclusions. Orthopyroxene is subhedral to anhedral and fine grained (<0.1 mm). Some magnetite grains are included in orthopyroxene. Clinopyroxene is euhedral to anhedral, fine to medium grained (0.1 to 0.15 mm) with greenish to pink pleochroism. Biotite is brownish and fine grained (<0.1 mm). Magnetite is fine grained and angular.

Granitic pegmatite (NM-16-1)

The sample is mainly composed of K-feldspar (50%), quartz (45%), and secondary epidote and zoisite (5%) with accessory magnetite and zircon. The K-feldspar (0.7 to 0.9 mm) and quartz (0.5 to 0.6 mm) are coarse grained and angular (Fig. 5G). Epidote and zoisite are fine grained and shows needle or rhombus morphology and occurs along the margin of recrystallized quartz and K-feldspar.

Diorite (NM-2-2)

Sample NM-2-2 is composed of plagioclase (40%), hornblende (38%), quartz (10%), clinopyroxene (5%), orthopyroxene (5%), biotite (2%) and magnetite

(2%) with accessory zircon and apatite (Fig. 5B). Plagioclase is medium grained (0.2 mm), and euhedral to anhedral. Hornblende is euhedral to subhedral and fine to medium grained (0.1 mm), greenish to brownish in color, with biotite along the margins. Clinopyroxene is greenish, fine to medium grained (0.1 to 0.2 mm), and subhedral to anhedral. Orthopyroxene is fine to medium grained (0.15 mm) and brownish. Biotite is dark brownish, subhedral to anhedral and fine to medium grained (0.1 mm). Magnetite is irregular and fine grained. Euhedral to subhedral apatite shows high relief and occurs as inclusions in plagioclase.

Amphibolite (NM-5-1, NM-5-2, NM-5-3, NM-8-2)

The rocks are mainly composed of hornblende (60%), plagioclase (35%), and biotite (5%), minor biotite and chlorite, with magnetite and zircon. Hornblende is medium grained (0.15 mm) and defines prominent foliation. Many grains are altered into chlorite or biotite. Plagioclase is fine grained and few large grains (0.2 mm) are commonly altered to sericite. Biotite is fine grained and greenish.

BIF (NM-14-1, NM-14-2, NM-15-1)

BIF samples are composed of magnetite (35-40%), quartz (30-35%), orthopyroxene (8-15%), biotite and hornblende (5%), clinopyroxene (3-5%) (NM-14-1, Fig. 6 A, B, C, D, E, H, I). Magnetite layers (<0.2 mm) alternate

between recrystallized quartz layers. Some magnetite grains are surrounded by red cherry hematite. Quartz is subhedral and fine grained and elongated. Orthopyroxene is fine grained and irregular, and is commonly intercalate in magnetite layers. In sample NM-14-3, the orthopyroxene is partially altered and some grains are rimmed by hornblende, which is included in magnetite in turn. Hornblende is fine grained and greenish and occurs both as inclusions in magnetite, or along the margin of magnetite layers. Sample NM-14-2 contains thicker layers of magnetite (up to 0.5 mm) and quartz (up to 0.6 mm) with both minerals showing prominent elongation.

BMQ (Banded magnetite quartzite) (NM-14-3, NM-14-4)

The BMQ are composed of magnetite (35%), quartz (40%), clinopyroxene (10-12%), orthopyroxene (5%), and hornblende (5-8%) (Fig. 6F, G). Magnetite band is thinner than in the previous sample, and magnetite grains are included in clinopyroxene. Quartz is fine grained and angular. Clinopyroxene is deformed and elongated as layers. Clinopyroxene and magnetite are intercalated within the layers. Some recrystallize quartz veins traverse the rock.

5. Geochemistry

Amphibolite

Amphibolites from Piranjunur and Matrapalli areas of NLSZ show wide variations for SiO_2 (40.2-52.9 wt. %), Al_2O_3 (2.15-15.22), Fe_2O_3 (9.2-35.9 wt.%), MgO (5.4-13.4 wt. %), CaO (3.3-6.8 wt.%) with low concentrations of TiO_2 (0.4-0.9 wt. %), MnO (0.1-0.2 wt.%) and P_2O_5 (0.1-0.3 wt.%). Total alkali contents widely varies from 7.1-8.8 wt.%. The studied samples straddle the fields of andesite/ basalt, andesite and rhyodacite/dacite on Zr/Ti vs. Nb/Y plot (Fig. 7A) suggesting intermediate to felsic magma compositions. In Zr vs. Y diagram (Fig. 7B, after Ross and Bedard, 2009) the amphibolites correspond to a transitional chemistry spanning over tholeiitic to calc-alkaline compositions for the parent magma. Transitional trace elements such as Ni: 50.7-252.4 ppm, Cr: 43.4-823.9 ppm show widely variable concentrations but overall depleted in comparison to primitive mantle values (Ni: >400 ppm, Cr: >800 ppm). Large Ion Lithophile Element (LILE) chemistry (Supplementary table 1) is marked by higher Sr (655.2-922.3 ppm) and Ba (395-1176 ppm) with relatively lower Rb (40.5-79.7 ppm) contents. These geochemical features in conjunction with well-developed troughs at Nb-Ta, Zr-Hf, Ti and positive anomalies at La-Ce-Pr-Nd on primitive mantle normalized trace element abundance (Fig. 8) patterns suggest distinct LILE-LREE enrichment and relative HFSE depletion for the studied amphibolites. Chondrite normalized REE patterns (Fig. 8) with $(La/Sm)_N$: 2.62-4.11, $(Ce/Yb)_N$: 9.9-18.5 and $(Gd/Yb)_N$: 2.2-3.01 corroborate pronounced LREE and MREE enrichment over HREE. The REE signature attests to prominent LREE/MREE,

MREE/HREE and LREE/HREE fractionations. Negative Eu anomalies suggest fractionation of plagioclase, while one sample with positive Eu anomaly indicate retention of plagioclase in the melt.

Diorite and granodiorite

Major oxide compositions for granodiorite and diorite samples from Appukottai, Karimangalam and Periyampatti areas of NLSZ is characterized by high SiO_2 (58.83-67.5 wt. %), moderate Al_2O_3 (13.6-16.9 wt. %), low to moderate Fe_2O_3 (1.9-9.5 wt.%), MgO (0.9-5.9 wt. %), TiO_2 (0.3-1.2 wt. %) and low MnO (0.01-0.11 wt.%), CaO (1.3-2.4 wt.%), P_2O_5 (0.1-0.4 wt.%) contents. Total alkali shows high concentrations ranging from 7.1 to 8.9 wt.%. Two granodiorite samples correspond to rhyodacite/dacite magma compositions, whereas the diorite sample shows andesitic nature on Zr/Ti vs. Nb/Y plot (Fig. 7A). The Zr vs. Y variations (Fig. 7B, after Ross and Bedard, 2009) for reflect transitional to calc-alkaline nature of parent melts. Transitional trace elements show extremely depleted concentrations (Ni: 1.2-4.7 ppm, Cr: 12.2-161.8 ppm) with respect to primitive mantle values (Ni: >400 ppm, Cr: >800 ppm). Among Large Ion Lithophile Elements (LILE), the studied samples are characterized by higher Sr (407.8-767.2 ppm) and Ba (169.9-1281.3 ppm) with relatively lower Rb (5.9-83.1 ppm) contents. Primitive mantle normalized trace element abundance (Fig. 8) patterns reflect negative anomalies at Nb-Ta, Zr-Hf, Ti and positive anomalies at La-Ce-Pr-Nd thereby attesting to LREE enrichment and

relative depletion in HFSE. Chondrite normalized REE patterns (Fig. 8) for the studied samples show sharp LREE/MREE, LREE/HREE and MREE/HREE fractionation trends. $(La/Sm)_N$: 3.4-7.3, $(Ce/Yb)_N$: 12.2-50.55 and $(Gd/Yb)_N$: 1.99-3.7 substantiate distinct LREE and MREE enrichment over HREE. Negative Eu anomalies for granodiorite suggest fractionation of plagioclase in the parent melt, where diorite sample showing positive Eu anomaly conform to plagioclase crystallization.

Hornblende-garnet-biotite gneisses and charnockite

The hornblende-garnet-biotite gneisses and charnockites from the study area can be compositionally classified as intermediate type with SiO_2 content ranging from 52 wt. % to 69 wt. % with moderate TiO_2 (0.3-1.8 wt.%), Al_2O_3 (13.1-15.4 wt.%) and Fe_2O_3 (2.5-12.2) contents. In terms of total alkali vs. silica (Fig. 9A) variations, the intermediate charnockites correspond to granite, granodiorite and syenodiorite compositions, while the gneisses show compositional affinity towards, granite, syenodiorite and syenite. On CaO-Na_2O-K_2O plot the charnockites and gneisses straddle the fields for granodiorite and quartz monzonite (Fig. 9B). In terms of alumina saturation index, these charnockites and gneisses are low peraluminous type (Fig. 9C) and show variations from calc-alkalic to alkalic in terms of modified alkali-lime index (Fig. 9D). The charnockites and gneisses are magnesian in terms of Fe-number (Fig. 10A) and have high MgO content (1.00 wt. %-6.31 wt.%). The

trace element chemistry for these rocks are marked by depleted concentrations for transitional trace elements (Ni, Co and Cr) and HFSE with respect to LILE and LREE. Primitive mantle normalized trace element patterns reflect distinct negative anomalies at Nb-Ta with distinct LREE enrichment (Fig. 8). Chondrite normalized REE patterns (Fig. 8) show pronounced LREE enrichment with flat HREE patterns. The studied samples with $(La/Sm)_N$: 2.3-10.14, $(La/Yb)_N$: 2.6-89.8 and $(Gd/Yb)_N$: 0.3-3.9 show sharp LREE/MREE, LREE/HREE and MREE/HREE fractionation trends. Most of the samples show negative Eu anomalies except charnockite sample NM-4-1 and gneiss sample NM-16-2.

Banded Iron Formation

The BIF samples from NLSZ are characterized by 17.8–33.6 wt.% SiO_2 and 64.8-77.8 wt.% Fe_2O_3. ΣREE of the studied samples exhibits a wide variation from 9.2 to 44.2 ppm with Y abundances varying between 4.8 and 18.1 ppm. Majority of the BIF samples show superchondritic Y/Ho ratios up to 29. Post-Archean Australian Shale (PAAS) normalized REE patterns (Fig. 8) depict positive La and Eu anomalies with negative Ce and Yb anomalies Among transitional trace elements, the BIF samples show low Ni, Cr, Co and Sc concentrations with variable enrichment in Vanadium. The large ion lithophile element (LILE) compositions are marked by low Rb and Cs contents and elevated Sr and Ba concentrations (Supplementary table 1). High field

strength element (HFSE) contents are low in these samples except for the relatively higher concentrations of Y.

BMQ (Banded magnetite quartzite)

Major element chemistry of BMQ rocks from the Arasakanni area of the NLSZ is marked by low concentrations of SiO_2 (39.9-40.85 wt. %) with pronounced enrichment of Fe_2O_3 (52.9-53.1 wt.%). ΣREE of the studied samples range from 35.23 ppm to 64.41 ppm with Y contentration varying between 14.87 and 16.45 ppm. Majority of the BMQ samples show superchondritic Y/Ho ratios up to 32. Post-Archean Australian Shale (PAAS) normalized REE patterns (Fig. 8) depict positive Eu anomalies. The BMQ samples show low Co and Sc concentrations with variable enrichment in Vanadium. The large ion lithophile element (LILE) compositions display low Rb and Cs contents and elevated Sr and Ba concentrations (Supplementary table 1).

6. U-Pb geochronology

Ten representative samples from the different rock types were analyzed for zircon U-Pb geochronology. Representative CL images of the zircon grains are shown in Fig. 16 and the U-Pb age data are given in Supplementary table 2 and plotted in Figs. 15-17. Zircon REE results are given in Supplementary table 3 and plotted in Figs. 18 and 19.

6.1 Zircon morphology

Meta-monzogranite (NM-8-1)

Zircon grains from sample NM-8-1 are dark brownish and euhedral to subhedral. Most of the grains are prismatic or stumpy, and few grains display rounded shape (Fig. 14A). They range in length from 60 to 150μm, with aspect ratios of 2:1 to 1:1. Under cathode luminescence image, core- rim texture is common with the high U dark magmatic core displaying relict oscillatory or sector zoning and surrounded by metamorphic rim (up to 50μm). Structureless high luminescence metamorphic grains are also present. Some xenocrystic cores are surrounded by overgrowth mantle, which is in turn are rimed by an irregular metamorphic overgrowth, indicating marginal resorption and reprecipitation. Minor inherited cores are heterogeneous.

Amphibolite (NM-5-1)

Zircon grains from samples NM-5-1 are transparent or dark brownish, and subhedral to anhedral. Rounded to subrounded grains are common (Fig. 14D). They range in length from 70 to 200 μm, with aspect ratios of 2:1 to 1:1. In CL, the grains display core-rim texture with a dark magmatic core surrounded by irregular metamorphic rim (up to 120μm). Homogenous and unzoned metamorphic grains also occur. Some magmatic cores are structureless, and

some show patchy zoning. The overgrowth metamorphic rims are irregular indicating resorption and reprecipitation.

Granodiorite (NM-3-1)

Zircon grains from sample NM-3-1 are transparent and some grains contain acicular inclusions. Most of the grains are prismatic or stumpy with a size range of 100-210μm and aspect ratios of 3:1-1:1 (Fig. 14E). In CL, core-rim structure is obvious, with magmatic cores are surrounded by metamorphic rims (up to 50μm). Some magmatic cores show oscillatory zoning or sector zoning. Heterogeneous cores also exist. Metamorphic rims are of two types: a regular overgrowth or discontinuous zone enveloping the magmatic cores. Xenocrystic cores are also present which are mantled by overgrowth rim, and further surrounded by a thin metamorphic rim. Structureless and homogenous metamorphic grains are rare.

Charnockite (NM-2-1)

Zircon grains from sample NM-2-1 are transparent and pinkish or brownish, euhedral to anhedral. Some grains are prismatic or stumpy, whereas others are rounded to subrounded (Fig. 14B). The grain size ranges from 80μm to 200μm, with aspect ratios of 2.5:1 to 1:1. Core-rim texture is common and the metamorphic rims show variable thickness of up to 100μm. Most zircon grains are heterogeneous and consist of dark and bright domains. Few magmatic

cores show oscillatory zoning. Minor grains preserve small xenocrystic core with an overgrowth mantle, which is surrounded by a metamorphic rim. Most of the metamorphic rims are regular.

Diorite (NM-2-2)

Zircon grains from sample NM-2-2 are transparent or brownish, subhedral to anhedral, and some grains are rounded to subrounded (Fig. 14C). They are relatively small (50-150μm in length, 30-80μm in width), and show aspect ratios of 3:1 to 1:1. In CL, the magmatic cores are dark and enclosed by irregular metamorphic rim (up to 40μm). Several magmatic cores show partly high luminescence domains. Some metamorphic grains are polyphase and consist of dark and high luminescence domains.

Garnet-bearing charnockite (NM-16-2)

Zircon grains from sample NM-16-2 are brownish and some are transparent, prismatic to stumpy (Fig. 14F). Their grain size show a range of 50-160μm, with aspect ratios of 2:1-1:1. Most of the grains show core-rim texture, with metamorphic rim up to 80μm in width. Several grains are unzoned and homogenous. Oscillatory zoning in the core is invisible due to their high uranium content. In transmitted light, many grains are fractured.

Granitic pegmatite (NM-16-1)

Zircon grains from sample NM-16-1 are brownish or transparent, and euhedral to subhedral. Some grains are rounded to subrounded, and few are prismatic in morphology (Fig. 14J). The grains show variable size 50-150μm, with aspect ratios of 3:1 to 1:1. Most of the grains display faint oscillatory zoning in the core which are surrounded by irregular dark overgrowth rim, and rimed by thin zigzag overgrowth. Few grains display oscillatory zoning and high luminescence. Minor grains preserve small xenocrystic cores (up to 30μm).

BIF (NM-14-1, NM-14-2)

Zircon grains from the BIF are transparent and few are brownish showing angular morphology (Fig. 14G, I). Minor grains are rounded in shape. The grains size is variable 35×30μm -100×110μm, with aspect ratios of 1.5:1 to 1:1. In CL, most gains show weak discontinuous oscillatory zoning or patchy zoning. Unzoned and homogenous grains are common. Minor grain shows core-rim texture with the magmatic core surrounded by metamorphic rim and is a xenocryst.

BMQ (NM-14-3)

Only few zircon grains were obtained from sample NM-14-3, and they are mostly transparent and colorless. The grain size is small and variable, 25×25μm-50×100μm, with aspect ratios of 2:1 to 1:1. Some grains show core-

rim texture, the metamorphic domains show variable width (up to 50μm). High luminescence unzoned grains are also present.

6.2 Zircon U-Pb data

Meta-monzogranite (NM-8-1)

Sixty grains were analyzed from sample NM-8-1, and excluding twenty two grains showing low concordance, the remaining data can be divided into three groups. One xenocrystic core yielded a weighted mean $^{207}Pb/^{206}Pb$ age of 3195±69 Ma and the Th, U contents are 173 ppm and 351 ppm. The second group contains seven grains among which five concordant grains show weighted mean $^{207}Pb/^{206}Pb$ age of 2714±29/62 Ma (n=5, MSWD=0.62) (Fig. 15A). Their Th, U contents are 298-475 ppm and 332-532 ppm. The third magmatic group contains twenty five grains among which twenty one concordant grains yield $^{207}Pb/^{206}Pb$ age of 2565±14/53 Ma (n=21, MSWD=0.25). Their Th contents range from 145 ppm to 532 ppm and U contents range from 124 ppm to 676 ppm. The metamorphic group contains five grains which show weighted mean $^{207}Pb/^{206}Pb$ age of 2536±34/61 Ma (n=5, MSWD=0.43) (Fig. 15B). Their Th, U contents are slightly lower as 122-393 ppm and 54-115 ppm. The magmatic zircon grains are characterized by steep LREEE to HREE pattern with negative Eu anomalies, whereas the metamorphic grains show HREE depletion together with negative Pr, Eu anomaly and positive Ce anomalies (Fig. 18A).

Amphibolite (NM-5-1)

Totally thirty spots were analyzed on twenty eight grains among which three spots are excluded due to poor data quality. The remaining twenty seven grains can be divided into magmatic and metamorphic groups. Twelve spots with high concordance among twenty one spots of the magmatic group yield weighted mean $^{207}Pb/^{206}Pb$ age of 2559±19/55 Ma (n=12, MSWD=0.91) (Fig. 15C). Their Th, U contents are in the range of 65-210 ppm, 104-269 ppm. Another group includes six spots among which four concordant spots show $^{207}Pb/^{206}Pb$ age of 2493±67 Ma (n=4, MSWD=0.17) corresponding to the timing of metamorphism (Fig. 15D). They show low Th and U contents of 5-6 ppm and 14-17 ppm. The zircon REE patterns are characterized by negative Pr, Eu anomaly and positive Ce anomaly, with the magmatic grains showing higher contents in MREE and HREE (Fig. 18B).

Granodiorite (NM-3-1)

Thirty spots were analyzed from twenty six grains and excluding two spots with bad signal, the remaining twenty eight grains can be divided into magmatic and metamorphic groups. The magmatic group contains twenty two spots among which twenty spots yield weighted mean $^{207}Pb/^{206}Pb$ age of 2553±15/53 Ma (n=20, MSWD=0.73) (Fig. 15E). Their Th and U contents are 94-280 ppm and 122-354 ppm. The metamorphic group includes six spots

among which four concordant spots define a weighted mean $^{207}Pb/^{206}Pb$ age of 2511±44/67 Ma (n=4, MSWD=0.29) (Fig. 15F). Compared with the magmatic grains, they show lower Th, U content of 29-109 ppm and 44-226 ppm. Most of the magmatic zircon grains show negative Pr, Eu anomaly and positive Ce anomalies, with steep LREE to HREE patterns (Fig. 18C).

Charnockite (NM-2-1)

Thirty one spots were analyzed on twenty seven grains and can be divided into magmatic and metamorphic groups. The magmatic group contains twenty three grains from which twenty concordant grains yield a weighted mean $^{207}Pb/^{206}Pb$ age of 2518±14/52 Ma (n=20, MSWD=0.39) (Fig. 16A). Their Th, U contents are 133-334 ppm and 136-216 ppm. The metamorphic group includes eight spots from which five concordant spots show weighted mean $^{207}Pb/^{206}Pb$ age of 2476±45/67 Ma (n=5, MSWD=0.16) (Fig. 16B). They yield slightly lower Th, U contents of 92-146 ppm and 31-63 ppm. Both the magmatic and metamorphic zircon grains display negative Pr, Eu anomaly and positive Ce anomaly, with the magmatic grains possessing higher MREE and HREE (Fig. 18D).

Diorite (NM-2-2)

Thirty one spots were analyzed on thirty one grains and can be divided into magmatic and metamorphic groups. The magmatic group contains twenty

grains from which nineteen high concordance grains yield weighted mean $^{207}Pb/^{206}Pb$ age of 2511±15/32 Ma (n=19, MSWD=0.23) with variable Th, U content of 111-1011 ppm and 54-3007 ppm (Fig. 16C). The metamorphic group contains eleven spots and ten spots yield a weighted mean $^{207}Pb/^{206}Pb$ age of 2475±24/55 Ma (n=10, MSWD=0.072) (Fig. 16D). Their Th, U content are in the range of 11-291 ppm and 18-234 ppm. The zircon REE pattern show negative Pr, Eu anomaly and positive Ce anomalies with most of the metamorphic grains showing lower HREE as compared to the magmatic grains (Fig. 18E).

Grt-bearing charnockite (NM-16-2)

Forty grains were analyzed from sample NM-16-2, excluding one spot, the remaining thirty nine spots can be divided into two groups. The magmatic group contains thirty spots among which twenty two concordant data yield weighted mean $^{207}Pb/^{206}Pb$ age of 2514±14/52 Ma (n=22, MSWD=0.37) (Fig. 17A). Their Th, contents are in the range of 17-247 ppm, and U contents are very high 245-2443 ppm. The metamorphic group contains nine spots and eight spots display weighted mean $^{207}Pb/^{206}Pb$ age of 2506±27/57 Ma (n=8, MSWD=0.23) (Fig. 17B). Their Th, U contents are 71-97 ppm, 52-81 ppm. The magmatic and metamorphic grains from this show negative Pr and Eu anomaly and positive Ce anomaly, with no clear distinction in HREE concentration of the magmatic group (Fig. 19A).

Granitic pegmatite (NM-16-1)

Forty five grains were analyzed for zircon U-Pb dating, and forty four grains yield weighted mean $^{207}Pb/^{206}Pb$ age of 2498±11/51 Ma (n=44, MSWD=0.39) (Fig. 16E). The Th, U contents show a variety of 1-460ppm, 65-574 ppm. The zircon REE pattern in this sample are variable and most of the magmatic grains show HREE enrichment and negative Pr, Eu anomaly and positive Ce anomaly. Few grains characterized by LREE enrichment (Fig. 18F).

BIF and BMQ (NM-14-1, NM-14-2, NM-14-3)

Totally thirty grains were analyzed from sample NM-14-1 and can be divided into two groups. The first group contains one grain and show $^{207}Pb/^{206}Pb$ age of 2550±76 Ma. The Th, U contents are 261 ppm, 184 ppm. Another group contains twenty nine grains among which twenty seven concordant grains display weighted mean $^{207}Pb/^{206}Pb$ age of 2464±13/51 Ma (n=27, MSWD=0.42) (Fig. 17C). Their Th, U contents are slightly higher and in the range of 31-117 ppm, 197-465 ppm. The zircon grains in this sample show a steep slope from LREE to HREE, and negative Pr, Nd anomaly and positive Ce anomaly (Fig. 19B). One magmatic xenocryst in this sample show slightly higher MREE.

Totally twenty six grains were analyzed from sample NM-14-2, and excluding one spot, twenty five grains can be divided into two groups. One magmatic

grain shows $^{207}Pb/^{206}Pb$ age of 2533±60 Ma with Th, U contents of 226 ppm and 288 ppm. The other twenty four grains yield weighted mean $^{207}Pb/^{206}Pb$ age of 2470±13/51 Ma (n=24, MSWD=0.38) (Fig. 17D). They yield slightly low Th content of 42-130 ppm, and U content show a variety of 216-645 ppm. Zircon REE patterns show a steep slope of LREE/HREE, and negative Pr anomaly and positive Ce anomaly. One magmatic grain shows slightly flat pattern with LREE enrichment (Fig. 19C).

Fifteen grains were analyzed from sample NM-14-3, and excluding one spot due to its low concordance, the remaining fourteen grains can be divided into two groups. One group includes seven magmatic grains which show weighted mean $^{207}Pb/^{206}Pb$ age of 2483±31/59 Ma (n=7, MSWD=0.28) (Fig. 17E). Their Th, U contents range from 22 ppm to 676 ppm and 133 ppm to 1964 ppm. Another group includes seven metamorphic grains and five grains from these show weighted mean $^{207}Pb/^{206}Pb$ age of 2460±42/65 Ma (n=5, MSWD=0.064) (Fig. 17F). Their Th, U contents are slightly lower 14-218 ppm, 14-651 ppm. The zircon REEs in this sample show LREE depletion, and negative Pr, Eu anomaly and positive Ce anomaly. Some magmatic grains show higher LREE (Fig. 19D).

6.3 Zircon Lu-Hf results

Zircon grains from seven samples were analyzed for Lu-Hf and the results are plotted in Fig. 20. The data are given in Supplementary table 4.

Meta-monzogranite (NM-8-1)

Three spots from sample NM-8-1 for Lu-Hf isotopes cluster into two groups based on their formation time. One spot from the 2714±62 Ma group yields higher $^{176}Hf/^{177}Hf_i$ values of 0.281105, $^{176}Lu/^{177}Hf$ 0.0009, together with positive εHf(t) of +2.0, its T_{DM}^{C} is 3043 Ma. Another two spots in the 2565±53 Ma age group show $^{176}Hf/^{177}Hf_i$ values of 0.281058 and 0.281077, and $^{176}Lu/^{177}Hf$ 0.0011 and 0.0004, with negative εHf(t) values of -3.1 and -2.4. Their T_{DM}^{C} ages are 3240 Ma and 3200 Ma.

Amphibolite (NM-5-1)

Six spots were analyzed from sample NM-5-1 for Lu-Hf isotopes. Their $^{176}Hf/^{177}Hf_i$ values show a range of 0.281206-0.281309, $^{176}Lu/^{177}Hf$ 0.0003-0.0010, and positive εHf(t) values of +2.0 to +5.7 falling above the CHUR line. The T_{DM}^{C} age range from 2698 Ma to 2922 Ma and T_{DM} ages of 2645-2784 Ma, when calculate by zircon crystallization age of 2559±55 Ma.

Granodiorite (NM-3-1)

Seven spots were analyzed from sample NM-3-1 and the results show $^{176}Hf/^{177}Hf_i$ values of 0.281071-0.281181, $^{176}Lu/^{177}Hf$ 0.0004-0.0008, and εHf(t) values range from -2.9 to +1.0 corresponding to T_{DM}^{C} ages of 2981-3220 Ma, when calculated by zircon crystallization age of 2553±53 Ma.

Charnockite (NM-2-1)

Six spots were analyzed from sample NM-2-1 and the data display $^{176}Hf/^{177}Hf_i$ values of 0.281131-0.281200, $^{176}Lu/^{177}Hf$ 0.0004-0.0007, and variable εHf(t) values of -1.6 to +0.9 together with T_{DM}^{C} ages of 2962-3112 Ma when calculated by zircon U-Pb age of 2518±52 Ma.

Diorite (NM-2-2)

Six spots were analyzed from NM-2-2 and which show $^{176}Hf/^{177}Hf_i$ values of 0.281160-0.281335, $^{176}Lu/^{177}Hf$ 0.0002-0.0011, and variable εHf(t) values of -0.7 to +5.5 corresponding to T_{DM}^{C} ages of 2672-3055 Ma and T_{DM} ages of 2611-2845 Ma when calculated by zircon U-Pb age of 2511±52 Ma.

Grt-charnockite (NM-16-2)

Seven analysis from sample NM-16-2 show $^{176}Hf/^{177}Hf_i$ values of 0.281088-0.281217, $^{176}Lu/^{177}Hf$ 0.0001-0.0006, and εHf(t) values range from -3.2 to +1.4. They yield T_{DM}^{C} ages of 2927-3209 Ma when calculated by zircon U-Pb age of 2514±52 Ma.

Granitic pegmatite (NM-16-1)

Eight spots were analyzed from NM-16-1 and show $^{176}Hf/^{177}Hf_i$ values of 0.281075-0.281155, $^{176}Lu/^{177}Hf$ 0.0002-0.0010, and negative εHf(t) values of -4.1 to -1.2. The data yield T_{DM}^{C} ages of 3072-3247 Ma when calculated by

zircon U-Pb age of 2498±51 Ma.

7. Discussion

7.1 Subduction-accretion-collision and petrogenesis

The lithological assemblages from NLSZ represents an evolutionary sequence from oceanic plate subduction, ocean basin closure and accretion at active continental margins to collision of two continental blocks, underthrusting and exhumation. The magnesian, calc-alkalic to alkalic character is typical of charnockites formed in a subduction-related setting associated with an active continental margin (Yang et al., 2016). On Rb-Sr-Ba plots, the charnockites and gneisses from NLSZ correspond to high Ba-Sr granitoids (Fig. 10B). The charnockites straddle the fields for Archean TTG and island arc fields on Sr/Y vs. Y plot (Fig. 10C), albeit the gneisses are restricted to the arc field. Plots of the samples in Figure 9C reflect a felsic peraluminous source for these rocks. Tectonic discrimination diagrams (Figs. 10D and 10E) corroborate a volcanic arc-related subduction-collision regime. TiO_2 vs. SiO_2 and P_2O_5 vs. SiO_2 plots for the charnockite and gneissic samples from NLSZ are shown in Fig. 11. The isotherms in Fig. 11A show Fe–Ti oxide saturation temperatures at >900 to >950 ^{o}C and apatite saturation

temperatures at 800- <900^{o}C. The high temperature correlates with continuous subduction of oceanic slab along a continental margin accompanied by HT magmatism and HT metamorphism, possible upwelling of lithospheric mantle through slab window, and melting of overlying lower crustal materials, which collectively contributed to the origin and emplacement of the charnockites and gneisses of NLSZ (e.g., Rajesh, 2012; Ma et al., 2013).

The mafic-intermediate-felsic volcano-plutonic association from NLSZ is distinctly characterized by elevated Ba-Sr contents with LREE enrichment and relative depletion in Nb-Ta, Zr-Hf and Ti in comparison with primitive mantle values. These geochemical features suggest subduction zone magmatism and generation of precursor magmas from a mantle source metasomatised by fluids, melts and sediments from a subducted oceanic lithosphere. The Mg# values range between 24.5 and 37.8 and transitional trace element concentrations are lower than primitive mantle values, suggesting an evolved nature of parent magma.

High Zr/Hf and Zr/Sm ratios for the studied samples substantiate the role of slab-dehydrated fluids in modifying the composition of a depleted mantle wedge peridotite in an active subduction environment. Elevated Ba/Th, Ba/Nb and Ba/La ratios in subduction zone magmas reflect distinct enrichment of LILE over LREE and HFSE thereby endorsing enrichment of sub-arc mantle

by influx of slab-dehydrated LILE-rich fluids. The LREE abundances are controlled by sediment input and their enrichment over HFSE attesting to contributions from subducted sediment towards mantle wedge metasomatism and generation of arc magmas. The feature of Ba/Th, Ba/Nb, Ba/La and Sr/La ratios relatively higher than Th/Nb and Th/Yb corroborate involvement of slab derived fluids in the process of magma generation (Elliott et al., 1997; Deng et al., 2015, Liu et al., 2017). Negative anomalies at Nb-Ta and Zr-Hf are equated with subduction zone magmatism and assimilation of relatively older continental crust. The geochemical signature of the studied rocks endorses addition of juvenile materials by subduction zone magmatism accompanied by reworking of older crustal components. On Th/Yb vs. Nb/Yb plot (Fig. 12A), the studied samples correspond to active continental margin settings with significant input from subduction components. The arc affinity of these rocks is also brought out by plots in Zr/Nb vs. Nb/Th (Fig. 12B) diagram. Hydrous melts and slab-derived fluids are generally thought to be the two main agents in subduction zones causing metasomatism of mantle wedge prior to partial melting. Hydrous melts transport both water-soluble and water-insoluble materials, whereas slab-derived fluids generally transport water-soluble materials (Jiang et al., 2017). In subduction zones, the Ba/La fractionation can only be reasonably achieved by elemental mobility in hydrous fluids, while Th and LREE are more immobile in fluids but mobile in melts than HREE and LILE (Woodhead et al., 2001). Therefore, elements such as Ba/La and

Th/HREE can be considered as useful tracers of sediment inputs or fluid contributions. The mafic-intermediate rocks of present study are characterized by higher Ba/La compared to Th/Yb indicating that the mantle source may be previously enriched by slab-derived fluids rather than hydrous melt. Plots of the samples in Nb/Zr vs. Th/Zr diagram (Fig. 12C) substantiate fluid-related enrichment of mantle wedge. The REE signature (Fig. 12D) of the rocks from NLSZ suggest low degree partial melting of a peridotitic mantle where garnet remained as a stable residual phase in the restite. The volcano plutonic lithologies of mafic-intermediate-felsic compositions might represent accreted and metamorphosed paleo-arc sections that record imprints of magmatic pulses, inter crustal differentiation processes like fractional crystallization, anatexis and reworking of older mid lower crustal continental rocks. The magmatic and metamorphic associations of NLSZ mark an oceanic sutures zone representing Alpine type paleo-subduction zones and preserve the history of continental amalgamations and orogenic process from ocean subduction, ocean basin closure, accretion, continental collision, under thrusting and exhumation to collapse.

7.2 Hydrothermal signature and depositional environment of BIFs

BIFs are classified into two types based on the sedimentary and tectonic

environments of their deposition (Gross, 1996). The Algoma-type BIF is smaller in size and thickness, associated with mafic/ultramafic to felsic volcanic rocks or volcaniclastic rocks and greywackes and deposited in arc/backarc basins or intracratonic rift zones. In contrast, the Superior-type BIF is thicker, occur in association with clastic–carbonate rocks and deposited in shallow marine conditions during transgressive phase, on the continental shelves of passive tectonic margins or in intracratonic basins. Transition type BIFs are characterized by a transitional depositional regime shifting between continental shelves and deep water regions (González et al., 2009). The BIFs and BMQs of NLSZ have low concentrations of Al_2O_3 and TiO_2 (wt. %) with marked depletion in HFSE. These geochemical features indicate minimum contributions from detrital components and negligible effect of contamination through clastic/crustal materials during precipitation. The PAAS-normalized REE patterns (Fig. 8) exhibit LREE depletion with positive La and Eu anomalies and superchondritic Y/Ho ratios, similar to those of modern seawater (German et al., 1995; Alibo and Nozaki, 1999). Positive Eu anomalies of these BIFs and BMQs provide evidence for submarine high-T (N350 °C) hydrothermal fluid input (Bau and Dulski, 1999; Zhu et al., 2015). Plots in the SiO_2 vs. Al_2O_3 diagram (Fig. 13A) suggest a genetic link of NLSZ BIFs and BMQs with submarine hydrothermal activity. The elevated abundances of trace elements like Ba, Sr, V, Zn in the studied BIF and BMQ samples indicate partitioning of these elements into ferric oxyhydroxides. This

observation implies that these trace elements were deposited on the sea floor with ferrihydrite particles and upon burial, they were remobilized followed by resorption onto ferrous-iron containing minerals. Majority of the studied BIF samples are marked by low Th/U ratios (Fig. 13B) reflecting feeble effects of weathering and excluding the possibility of phosphate contamination. The positive Eu anomalies of these BIFs and BMQs in combination with decreasing abundance from LREE to HREE and low Al_2O_3 contents reflect the role of high silica-low alumina hydrothermal solutions in precipitating alumina-poor iron silicates. According to the depositional models for BIFs (Rasmussen et al., 2013), the Fe-rich layers of NLSZ BIFs were deposited by oxidation of ferrous iron from paleo-ocean and precipitation of insoluble ferric oxyhydroxides, while the Si-rich layers were formed by removal of silica dissolved in Precambrian seawater by abiotic processes. Alexander et al. (2008) evaluated the proportion of modern seawater and high-T hydrothermal fluids through Sm/Yb–Eu/Sm relationship which indicates that extremely small amounts of submarine high-T hydrothermal fluids (~0.1%) are enough to yield strong positive Eu anomalies (Fig. 13C). Based on these geochemical features, the NLSZ BIFs and BMQs are considered to be the products of chemical sedimentation from paleo-seawater enriched in dissolved Fe and Si with significant input of volcanic hydrothermal fluids. Eu anomalies in BIFs and BMQs are believed to originate in the stratified oxygen deficient bottom waters where reduction of Eu^{3+} to Eu^{2+} takes place during hydrothermal

alteration. The discharging hydrothermal fluid becomes enriched in Eu because of low sorption of Eu^{2+} compared to other REEs (Bau and Dulski, 1999). The pronounced positive Eu anomalies and superchondritic Y/Ho ratios of NLSZ BIFs and BMQs imply distinct seawater signatures. Negative to no Ce anomalies, depleted ΣREE and positive Eu anomalies in these BIFs and BMQs collectively suggest that their metal content was added to ambient oceans by hydrothermal solutions at hydrothermally active ocean-continent convergent margin environment.

7.3 Magma provenance from zircon data

The Lu-Hf isotopes of the magmatic zircon grains which define emplacement age of 2565 Ma for the protolith of sample NM-8-1 meta-monzogranite show slightly negative εHf(t) values between -3.1 and -2.4 corresponding to $^{176}Hf/^{177}Hf_i$ values range from 0.281058 to 0.281077 and low $^{176}Lu/^{177}Hf$ 0.0011 and 0.0004 (lower than 0.015, Amelin et al., 1999). The data indicate that the magma was sourced by the reworking of an older crustal source. However, the positive εHf(t) value of +2.0 for the 2714 Ma group together with higher $^{176}Hf/^{177}Hf_i$ value of 0.281105, $^{176}Lu/^{177}Hf$ of 0.0009 (lower than 0.022, Griffin et al., 2002), indicate a juvenile source for the magma. This is coherent with the field observation with amphibolites occurring as enclaves within the meta-monzogranite suggesting magma mixing and mingling between mafic and felsic magmas. The 2565 Ma group might

therefore represent recrystallized zircons. However, the uniformly positive εHf(t) values of zircon grains from the amphibolite (NM-5-1) in the range of +2.0 and +5.7, together with higher $^{176}Hf/^{177}Hf_i$ values of 0.281206-0.281309 and moderate $^{176}Lu/^{177}Hf$ values 0.0003-0.0010, indicate a homogenous juvenile source. This could be mafic lower crust from underplated basalts derived through subducted slab melting, analogous to new crust generated in modern island arcs (see Fig. 20) (Dhuime, 2011).

Zircon Lu-Hf isotopes from the charnockite (NM-2-1, NM-16-2) and granodiorite (NM-3-1) show variable εHf(t) values of -3.2 to +1.4 and are dominantly negative, with $^{176}Hf/^{177}Hf_i$ values 0.281071-0.281217, and $^{176}Lu/^{177}Hf$ between 0.0001 and 0.0008. The data suggest that the magma was heterogeneous and included both reworked old crust and juvenile lower crust sources. The positive εHf(t) values from the granitoids indicate the magma are juvenile source.

The εHf(t) values from granitic pegmatite (NM-16-1) are negative, in the range of -4.1 to -1.2 with $^{176}Hf/^{177}Hf_i$ values are 0.281075-0.281155, $^{176}Lu/^{177}Hf$ 0.0002-0.0010, indicating reworked crustal source. The melts might have been extracted from the associated charnockites magma and emplaced at 2498 Ma.

The zircon εHf(t) values from diorite (NM-2-2) are variable (-0.7 to +5.5) and dominantly positive, which is close to the value of new crust and depleted

mantle line. Together with $^{176}Hf/^{177}Hf_i$ values between 0.281160 and 0.281335, $^{176}Lu/^{177}Hf$ 0.0002-0.0011, the data suggest magma source from depleted mantle mixed with crustal components. As the diorite occurs as enclaves within the charnockite, mixing between mafic and felsic magmas is indicated.

Overall, the magmatic zircon grains suggest crustal reworking and recycling together with the addition of juvenile magmas from depleted mantle sources which is typical of subduction-related magmatism in continental arc settings (e.g., Santosh et al., 2017). In the chondrite normalized REE diagrams, the magmatic zircons show high total REE contents, with the magmatic grains showing higher HREE than the metamorphic grains (Fig. 18 and 19). Compared with the metamorphic zircons, the magmatic grains show higher U contents (Fig. 21). As the least mobile element in zircon, we used Yb and Y for reference to trace the magma sources. In the U/Yb versus Y binary plot, most of the zircons fall in the continental field with minor grains showing oceanic zircon signature (Grimes et al., 2007). In the U versus Yb discrimination diagram, the zircon grains are characterized by continental crust feature (Fig. 19). The 'magmatic' zircon grains in the pelagic sediments (BIF) are considered to have been extracted from the intermixed oceanic basalt, with one zircon located in the oceanic crust and MORB field.

7.4 Implications of zircon U-Pb age data

We dated zircon grains in representative samples of all the major rock

types from the Nallamalai Suture Zone to constrain the timing of magmatism and metamorphism within this subduction-collision zone. The meta-monzogranite sample NM-8-1 yielded four age groups: the 3195±69 Ma represents inherited cores, and the 2714±29/62 Ma group corresponds to recrystallized mantles, and the emplacement of the protolith at 2565±14/53 Ma. The 2536±34/61 Ma age represents the timing of metamorphism. The granodiorite (NM-3-1) show emplacement at 2553±15/53 Ma immediately followed by metamorphism at 2511±44/67 Ma. The protolith of the charnockite (NM-2-1) was emplaced at 2518±14/52 Ma, and metamorphosed at 2476±45/67 Ma age. Another garnet-bearing charnockite (NM-16-2) shows protolith emplacement age as 2514±14/52 Ma and metamorphism at 2506±27/57 Ma. The granitic pegmatite (NM-16-1) marks the final phase of the thermal event, with an emplacement age of 2498±11/51 Ma, which is close to the metamorphic age from the other samples. These ages for protolith (magma) emplacement and high-grade metamorphism (>850 °C) are broadly identical and intruded into an already hot and deforming continental arc.

In comparison, the granitoids from the Shevaroy Block (the Salem Block) to the west show magma emplacement ages of 2758±16 Ma to 2530±9.4 Ma, with metamorphism during 2533±10 to 2530±15 Ma (Glorie et al., 2014). The tonalite, granite and charnockite from the Krishnagiri area to the north show

magmatic ages of 2557±16 Ma to 2529.9±4 Ma, and monazite metamorphic ages of 2517±10 Ma to 2506±10 Ma (Peucat et al., 1993). SHRIMP zircon age data from migmatites and charnockites of the Krishnagiri region also show magmatic ages of 2543±3 Ma and 2548±4 Ma, and metamorphism at 2515±9 Ma (Peucat et al., 2013). Charnockites from the Shevaroy massif show SHRIMP zircon magmatic age range from 2721±9 Ma to 2575±13 Ma and metamorphism at 2483±9 Ma (Peucat et al., 2013), Clark et al., (2009) reported SHRIMP zircon magmatic ages of 2538-2529 Ma, and metamorphic ages of 2482-2473 Ma from charnockite and associated leucosomes from the Salem Block, which forms part of the Shevaroy Bock. Charnockites from the Madras Block to the east of the Nallamalai Suture Zone yield magmatic ages between 2540±10 Ma and 2531±9.3 Ma (Glorie et al., 2014).

The diorite sample in our study (NM-2-2) shows 2511±15/32 Ma magmatic age and 2475±24/55 Ma metamorphism. The amphibolite (NM-5-1) shows 2559±19/55 Ma magmatic age and 2493±67 Ma metamorphic age. The BIF samples (NM-14-1, NM-14-2, NM-14-3) show metamorphic ages of 2464±13/51 Ma, 2470±13/51 Ma, 2483± 31/59 Ma, with two magmatic grains showing ages of 2550±76 Ma and 2533±60 Ma, which correlate with the age of magmatic zircon grains from the amphibolite, corresponding to oceanic crust. The peak age for magmatism of our samples is 2510 Ma and that for metamorphism is 2478 Ma (Fig. 21). The duration of magmatism from 2.7 to

2.5 Ga and metamorphism until 2.46 Ga compared with those in the adjacent Shevaroy and Madras Blocks (Fig. 23).

7.5 Crustal evolution

Our study area is located in an important tectonic divide between two crustal blocks: the Shevaroy Block to the West and the Madras Block to the east. Although previous studies designated this zone as the Nallamalai Shear Zone, it is evident from the lithological assemblages including continental and oceanic sequences that the transpressional shearing occurred along an oceanic suture zone. In order to further understand the tectonic history of this region, we briefly evaluate below the geochronological records from the surrounding crustal blocks.

To the north of the Nallamalai Suture Zone, the Dharwar Craton underwent two major continent growth events at 3.3 Ga and 2.7 Ga, and reworking around 3.0 Ga and 2.55-2.50 Ga (Lancaster et al., 2015), involving both juvenile magmas was formed around Mesoarchean and reworked components during Neoarchean. The ca.3.3 Ga TTG gneiss from the Western Dharwar Craton show εNd values in the range of -2.8 to +2.4, suggesting that the parent magma was derived from juvenile source with some older crust input (Jayananda et al., 2015). Detrital zircon with spot ages of 3161-3438 Ma

in the Western Dharwar Craton show positive εHf(t) values of +0.6 to +5.7, indicating derivation from magmatic sources constructed from juvenile components (Lancaster et al., 2015). The Mesoarchean continent growth is also preserved in other places, including the Coorg Block, where the εHf(t) from the granitoids and dioritic enclave display both positive and negative values of +5.1 to -4.8 and are dominantly positive suggesting magma mainly derived from juvenile source with nearly continuous continent growth through 3.5 to 3.1 Ga (Santosh et al., 2015) (Fig. 22). The Wynad region in the south west of our study area also preserved ca.3.3 Ga old crust and as well as the 2.5 Ga reworking component. However, limited addition of new crust also occurred during Neoarchean as suggested by the data from a metagabbro (ca.2.51 Ga) from Wynad region along the Moyar Suture Zone where zircon grains show positive εHf(t) values of +10.69 to +0.9, suggesting that the magma was extracted from the depleted mantle (Yano et al., 2016). Yang et al. (2016) reported detrital zircon grains in a quartzite from the Wynad region which show εHf(t) both positive and negative values of +5.24 to -4.86, when calculated by corresponding spot ages of 3043-3306 Ma, indicating both juvenile and reworked continent crustal components. Kumar et al., (2016) also reported similar data from quartzite in the Biligiri Rangan Block, immediately west of the Nallamalai Suture Zone, where zircon εHf(t) values show both positive and negative values of +5.1 to -6.4 and mostly positive when calculated by corresponding spot ages of 2972-3315 Ma, suggesting mixed

juvenile and reworked sources. However, the granitic rocks from this block with ca.2.5 Ga emplacement age yield negative εHf(t) values of -8.2 to -2.3 suggesting magma derivation from reworked older crust (Kumar et al., 2016) (Fig. 22).

In the Nilgiri Block to the south-west, the granitoids and amphibolite (ca.2.5 Ga) yield positive εHf(t) values of +0.8 to +9.3, indicating that the precursor magmas was derived from 2.6-2.8 Ga juvenile source during Neoarchean, similar to our Hf isotope results (Yang et al., 2015). Zircon grains in the granite carrying dioritic enclaves (ca.2.57-2.49 Ga) from the Kolar greenstone belt in the Dharwar Craton show positive εHf(t) values of +3.3 to +0.2, together with few grains showing negative values in the range of -3.1 to -0.1, suggesting magma derivation from both juvenile and reworked components (Yang and Santosh, 2015). Zircon grains from an amphibolite in Kolar show positive and negative values in the range of +5.1 to -5.0, and the precursor was derived from 2.7 Ga juvenile oceanic crust contaminated with the recycled continent crust (Yang and Santosh, 2015). The results are similar to those from our amphibolite sample (NM-5-1). The magmatic zircon grains from garnet-bearing migmatite and granitoids of the Shevaroy Block to the west of our study with εHf(t) values of +5.8 to -0.3 were also suggested to be derived from ~2.7-3.1 Ga juvenile crust (Glorie et al., 2014). Zircons in a granite in the Madras Block to the east of the Nallamalai Suture Zone show εHf(t) values of +5.1 to +0.1 with magma derivation correlate to ~2.7-3.1Ga

juvenile components (Glorie et al., 2014).

The granitoids in our study from the Nallamalai Suture Zone (ca. 2.71-2.50 Ga) show εHf(t) values in the range of -4.1 to +2.0 and the two stage model age T_{DM}^{C} of 2927-3247 Ma, indicating that the magma source involved reworked 2.9-3.2 Ga basement together with minor juvenile components. Zircons in the 2.51 Ga diorite (T_{DM}^{C} 2672-3055 Ma) and the 2.56 Ga amphibolite (T_{DM}^{C} 2698-2922 Ma) yield positive εHf(t) values, and the magmas were mainly extracted from juvenile ca.3.0-2.7 Ga continental and oceanic crust. Thus, continent growth is traced from 3.1 Ga to 2.7 Ga, corresponding to the basement of the two blocks to the west and east of the suture zone. To the north, the Dharwar Craton and associated microblocks experienced continent growth prior to 3.3 Ga which continued to 2.7 Ga.

7.6 Tectonic setting

Several distinct crustal blocks have been identified south of the Dharwar Craton in Peninsular India including the Coorg, Nilgiri, Biligiri Rangan, Shevaroy (Salem), and Madras Blocks from west to east (Kumar et al., 2016). Previous studies suggested that the Salem Block, Krishangiri region, and the Shevaroy massif belong to the Shevaroy Block (Glorie et al., 2014; Clark et al., 2009; Peucat et al., 1993, 2013). Part of the Salem Block was also considered to belong to the Madras Block (Glorie et al., 2014). However, the Shevaroy

Block and Madras Block are separated by the Nallamalai Suture Zone, from where we documented evidence for subduction-accretion and collision related rock suites. Thus, it is evidence that there were possibly several microblocks which were assembled along multiple zones of ocean closure at the end of Archean – earliest Paleoproterozoic, similar to the tectonic assembly reported from the North China Craton (Zhai and Santosh, 2011; Li et al., 2016). We further evaluate this aspect below from the various microblocks in the Dharwar Craton and surrounding region.

Recent studies based on precise isotopic geochronological techniques have led to the identification that the Dharwar Craton is composed of three distinct domains: the Western Dharwar Craton (>3.0 Ga), Eastern Dharwar Craton (2.5 to 2.7 Ga) and the Central Dharwar Craton (>3.0 Ga and 2.5-2.7 Ga) (Peucat et al., 2013; Lancaster et al., 2015). The Western Dharwar Craton and Eastern Dharwar Craton were welded along the Chitradurga Suture Zone located along the western periphery of the Central Dharwar Craton (Santosh and Li, 2018). Microblock amalgamation also occurred along oceanic suture zones in the southern periphery of the Dharwar Craton, including the assembly of Coorg Block at ca. 3.0 Ga, followed by the Nilgiri, Biligiri Rangan, Shevaroy and Madras Blocks in the Neoarchean (Yang et al., 2016; Kumar et al., 2016; Santosh et al., 2015; Samuel et al., 2014). The magmatic ages from the Shevaroy Block (comprising the Salem and Shevaroy Hills) are older than those of the Madras Block. Our field evidence

shows amphibolite in association with BIFs along the western margin of the Nallamalai Suture Zone adjacent to magmatic suite of meta-monzogranite, granitoids and charnockites suggesting subduction- accretion process followed by collision of the two blocks as represented by the late Neoarchean – early Paleoproterozoic metamorphic ages. The Hf isotopes also suggested increasing younger components in the magmatic suites from the west to east and the emplacement age of our charnockite samples are younger than those in the Shevaroy and Madras microblocks. The xenocrystic zircon cores in the meta-monzogranite might have been source from the basement of these blocks during subduction-related magmatism. The metamorphic age from the Shevaroy Block (peak metamorphism at 2.51 Ga) is older than the peak 2.48 Ga recorded from the Nallamalai Suture Zone (Fig. 23). The metamorphic age at 2555 ±140 from Madras Block interpreted to represent the granulite facies metamorphism (Bernard-Griffiths et al., 1987). Although only few data have been reported so far from the Madras Block, based on available information, we suggest an eastward subduction of the Shevaroy Block towards the Madras Block along the Nallamalai Suture Zone (Fig. 24).

Microblock amalgamation along multiple suture zones can be inferred from the information in previous studies in this region. Kumar et al., (2016) reported magmatic emplacement ages of 3189 Ma, 3019 Ma, and 2545 Ma from the BR Hills, with peak metamorphism at 2513 Ma (Peucat et al., 2013) (Fig. 23). From the Shevaroy Block, other workers reported magmatic

emplacement from 2758 Ma to 2514 Ma with few inherited cores of ca.3.2 Ga, followed by peak metamorphism at 2.5 Ga (Glorie et al., 2014; Peucat et al., 1993), with speculation that the Mettur Shear Zone might represent the zone of ocean closure (Fig. 23). Yang and Santosh, (2015) reported a suite rock types from the Kolar greenstone belt, including granite, diorite, amphibolite and BIF, with magmatism during 2581-2564 Ma, carrying inherited magmatic cores of 2718Ma to 2696 Ma, and metamorphism at ca.2.5 Ga. These ages are also close to the zircon and titanite ages from granodiorite gneiss and granitoids at 2631-2532 Ma, 2552 Ma to 2501 Ma (Balakrishnan et al., 1999). To the south of the Western Dharwar Craton, an exotic Mesoarchean block was identified - the Coorg Block which shows extensive magmatic crust building events during 3.3 Ga to 3.1 Ga, and metamorphism at ca. 3.0 Ga, without any imprint of the 2.5 Ga events widely documented in the surrounding blocks (Santosh et al., 2015). The Nilgiri Bock was constructed through extensive magmatism at 2.67 to 2.52 Ga, and metamorphism at 2.50 Ga (Peucat et al., 2013; Samuel et al., 2014). The Coorg Block amalgamated with the Western Dharwar during Mesoarchean, and the Nilgiri Block collided during Neoarchean (Santosh et al., 2015; Peucat et al., 2013; Yano et al., 2016).

Jayananda et al. (2013) reported Sm-Nd Grt-whole rock metamorphic ages from the Western Dharwar Craton (including Bababudan region, Holenarsipur region, Sargur-Gundlupet region), which show a range of 2527-

2414 Ma. The Central Dharwar Craton including the Bidaloti-Bandihalli and Rananagara-Kabbaldurga area shows metamorphism at 2550-2435 Ma (Jayananda et al., 2013). In the Hutti greenstone belt, monazite in tonalite gneiss shows metamorphic age at 2558 Ma close to the magmatic event in the Eastern Dharwar Craton (Jayananda et al., 2013). Thus, ca.2.55 Ga to ca.2.46 Ga metamorphism is widespread in the Dharwar Craton. The metamorphic peaks at 2478 Ma for Nallamalai Suture Zone, 2511 Ma for Shevaroy Block, 2532 Ma for Madras Block, 2452 Ma for the Kolar Greenstone Belt, 2500 Ma for BR Hills, 2513 Ma for Nilgiri Block, 2458 for Western Dharwar Craton, 2513 Ma for Eastern Dharwar Craton, 2378 Ma for Wynad Region all suggest multiple amalgamation of microblocks during the Archean- Paleoproterozoic transition in southern Peninsular India.

8. Conclusions

The following general conclusions can be drawn from the present study.

- Amphibolite-diorite-granodiorite assemblage from the NLSZ represent subduction-related magmatism at ocean-continent convergence associated with an active continental margin.
- Tholeiitic to calc-alkaline parental melts for mafic-intermediate-felsic compositions were generated by low degree partial melting of a peridotitic mantle wedge metasomatized by subduction-derived fluids

and sediments and continuous slab melting ensued by intracrustal fractional crystallization of melts with reworking of older continental crust.

- Gneisses and charnockites were derived from a felsic peraluminous source and emplaced in a subduction-collision regime.
- Geochemical characteristics of the BIF and BMQ samples including their positive Eu anomalies, negative to negligible Ce anomalies, and superchondritic Y/Ho ratios suggest that the BIFs were: (i) derived by chemical sedimentation from paleo-ocean enriched in dissolved iron and silica with marked contributions from hydrothermal fluids of volcanic origin, and (ii) deposited in an arc related off-shelf marine environment proximal to an active continental margin setting, where hydrothermal activity induced release of Eu and Y enriched hydrothermal solutions under low oxygen fugacity conditions.
- Geochemical signatures of NLSZ rocks conform to continental collision following subduction of intervening oceanic lithosphere and associated active continental margin magmatism and accretionary processes. Magmatic and tectonic attribute suggest that the NLSZ is an oceanic suture preserving the history of paleo-ocean, ocean-basin closure and amalgamation of continental blocks.

- Magmatic pulses within and adjacent to the NLSZ are recorded from

precise zircon geochronology at 2714±29/62 Ma and 2565±14/53 Ma from meta-monzogranite, 2553±15/53 Ma from granodiorite, 2518±14/52 Ma from charnockite, 2514±14/52 Ma from garnet-bearing charnockite, 2498±11/51 Ma from granitic pegmatite, 2511±15/32 Ma from diorite, and 2559±19/55 Ma from amphibolite. Metamorphism is dated at 2536±34/61 Ma for the meta-monzogranite, 2511±44/67 for granodiorite, 2476±45/67 Ma for charnockite, 2506±27/57 Ma for Grt-charnockite, 2475±24/55 Ma for diorite, 2493±67 Ma for amphibolite and 2464±13/51 Ma, 2470±13/51 Ma, 2460± 42/65 from BIFs and BMQs. The magmatic and metamorphic ages are very close, which is typical of many Archean terranes.

- The meta-monzogranite εHf(t) values from the 2714 Ma group shows positive value of +2.0, 2565 Ma group shows negative values of -3.1 and -2.4; the amphibolite yields positive values in the range from +2.0 to +5.7; the charnockite and granodiorite show variable values of -3.2 to +1.4; the granitic pegmatite displays negative values of -4.1 to -1.2; the diorite mainly shows positive values of -0.7 to +5.5. The data suggest that the juvenile crust growth in the continental arc basement started before 3.3 Ga and continued to 2.7 Ga.

- We suggest an eastward oceanic subduction and ocean closure

during along the Nallamalai Suture Zone welding the Shevaroy and Madras Blocks.

- Multiple subduction and amalgamation of several microblocks occurred in the Dharwar Craton and its southern domains, amalgamating several microblocks during the Archean – Paleoproterozoic transition.

Acknowledgements

We thank Prof. G.C. Zhao, Editor for his encouragement and two anonymous referees for providing us with constructive comments which helped in improving our paper. This study forms part of the PhD research of Shan-Shan Li at the China University of Geosciences Beijing. This work was funded by Foreign Expert Grants to M. Santosh by the CUGB, and also contributes to his Professorial position at the University of Adelaide, Australia. Sohini Ganguly acknowledges DST INSPIRE Faculty project [IFA 14-EAS-25] for financial support.

References

Alexander, B.W., Bau, M., Andersson, P., Dulski, P., 2008. Continentally derived solutes

in shallow Archean seawater: rare earth element and Nd isotope evidence in iron formation from the 2.9 Ga Pongola supergroup, South Africa. Geochimica et Cosmochimica Acta 72, 378–394.

Alibo, D.S., Nozaki, Y., 1999. Rare earth elements in seawater: particle association, shale normalization, and Ce oxidation. Geochimica Cosmochimica Acta 63, 363–372.

Amelin, Y., Lee, D.C., Halliday, A.N., Pidgeon, R.T., 1999. Nature of the Earth's earliest crust from hafnium isotopes in single detrital zircons. Nature 399, 252–255.

Balakrishnan, S., Rajamani, V., Hanson, G.N., 1999. U-Pb ages for zircon and titanite from the Ramagiri Area, Southern India: Evidence for accretionary origin of the Eastern Dharwar Craton during the Late Archean. The Journal of Geology 107, 69-86.

Bau, M., Dulski, P., 1999. Comparing yttrium and rare-earth in hydrothermal fluids from the mid-Atlantic ridge: implications for Y and REE behaviour during near vent mixing and for the Y/Ho ratio of Proterozoic seawater. Chemical Geology 155, 77–90.

Bernard-Griffiths, J., Jahn, B.M., Sen, S.K., 1987. Sm–Nd isotopes and REE geochemistry of Madras granulites, India: an introductory statement. Precambrian Research 37, 343–355.

Cawood, P.A., Strachan, R.A., Pisarevsky, S.A., Gladkochub, D. P., Murphy, J.B., 2016. Linking collisional and accretionary orogens during Rodinia assembly and breakup: Implications for models of supercontinent cycles. Earth and Planetary Science Letters 449, 118-126.

Chadwick, B., Vasudev, V.N., Hegde, G.V., 2000. The Dharwar craton, southern India,

interpreted as the result of Late Archaean oblique convergence. Precambrian Research 99, 91–111.

Chardon, D., Jayananda, M., Peucat, J.J., 2011. Lateral constrictional flow of hot orogenic crust: Insights from the Neoarchean of south India, geological and geophysical implications for orogenic plateau. Geochemistry Geophysics Geosystems 12 (2).

Clark, C., Collins, A. S., Timms, N. E., Kinny, P. D., Chetty, T. R. K., Santosh, M., 2009. SHRIMP U–Pb age constraints on magmatism and high-grade metamorphism in the Salem Block, Southern India. Gondwana Research 16(1), 27-36.

Clift, P. D., Vannucchi, P., Morgan, J. P. 2009. Crustal redistribution, crust–mantle recycling and Phanerozoic evolution of the continental crust. Earth-Science Reviews, 97, 80–104.

Collins, A.S., Clark, C., Plavsa, D., 2014. Peninsular India in Gondwana: The tectonothermal evolution of the Southern Granulite Terrain and its Gondwanan counterparts. Gondwana Research 25, 19-203.

Cox, K.G., Bell, J.D., Pankhurst, R.J., 1979. The Interpretation of Igneous Rocks. George, Allen and Unwin, London, p. 450.

Condie, K. C., 2005. High field strength element ratios in Archean basalts: a window to evolving sources of mantle plumes?. Lithos, 79(3-4), 491-504.

Crawford, A.R., 1969. India, Ceylon and Pakistan: New age data and comparisons with Australia. Nature 223, 380-384.

Deng, Y., Yuan, F., Zhou, T., Xu, C., Zhang, D., Guo, X., 2015.Geochemical

characteristics and tectonic setting of the Tuerkubantao mafic-ultramafic intrusion in West Junggar, Xinjiang, China. Geoscience Frontiers 6, 141-152.

Dhuime, B., Hawkesworth, C., Cawood, P., 2011. When continents formed. Science 331, 154-155.

Dhuime, B., Hawkesworth, C.J., Cawood, P.A. and Storey, C.D., 2012. A change in the geodynamics of continental growth 3 billion years ago. Science, 335, 1334–1336.

Drummond, M.S., Defant, M.J., 1990. A model for trondhjemite-tonalitedacite genesis and crustal growth via slab melting: Archaean to modern comparisons. Journal of Geophysical Research 95, 21503-21521.

Drury, S. A., Harris, N. B. W., Holt, R. W., Reeves-Smith, G. J., Wightman, R. T., 1984. Precambrian tectonics and crustal evolution in South India. Journal of Geology 92(1), 3-20.

Elliott, T., Plank, T., Zindler, A., White, W., Bourdon, B., 1997. Element transport from slab of volcanic front at the Mariana arc. Journal of Geophysical Research 102, 14991–15019.

Frost, B. R., Barens, C. G., Collins, W. J., Arculus, R. J., Ellis, D. J., Frost, C. D., 2001. A geochemical classification for granite rocks. Journal of Petrology 42, 2033–2048.

Geological Survey of India Calcutta, 1987, Geological Quandrange map:.Tiruppattur Quadrangle Tamilnadu-Andhra Pradesh-Karnataka. Geological Survey of India, Calcutta.

German, C.R., Masuzawa, T., Greaves, M.J., Elderfield, H., Edmond, J.M., 1995. Dissolved rare earth elements in the Southern Ocean: cerium oxidation and the

influence of hydrography. Geochimica et Cosmochimica Acta 59, 1551–1558.

Glorie, S., Grave, J. D., Singh, T., Payne, J. L., Collins, A. S., 2014. Crustal root of the Eastern Dharwar Craton: zircon U–Pb age and Lu–Hf isotopic evolution of the East Salem Block, southeast India. Precambrian Research 249(4), 229-246.

González, P.D., Sato, A.M., Llambías, E.J., Petronilho, L.A., 2009. Petrology and geochemistry of the banded iron formation in the Eastern Sierras Pampeanas of San Luis (Argentina): implications for the evolution of the Nogolí Metamorphic Complex. Journal of South American Earth Science 28, 89–112.

Green, T.H., Pearson, N.J., 1986. Ti-rich accessory phase saturation in hydrous mafic-felsic compositions at high P, T. Chemical Geology 54, 185–201.

Griffin, W.L., Wang, X., Jackson, S.E., Pearson, N.J., O'Reilly, S.Y., Xu, X., Zhou, X., 2002. Zircon chemistry and magma mixing, SE China: in-situ analysis of Hf isotopes, Tonglu and Pingtan igneous complexes. Lithos 61, 237–269.

Grimes, C.B., John, B.E., Kelemen, P.B., Mazdab, F.K., Wooden, J.L., Cheadle, M.J., Hanghøj, K., Schwartz, J.J., 2007. Trace element chemistry of zircons from oceanic crust: a method for distinguishing detrital zircon provenance. Geology 35, 643–646.

Gross, G.A., 1996. Algoma-Type Previous Term Iron-Formation. Next Term. In: Lefebure, D., Hõy, T. (Eds.), Selected British Columbia Mineral Deposits Profiles2. Ottawa British Columbia Ministry of Employment and Investment Open File, 25–28.

Harrison, T.M., and Watson, E.B., 1984. The behavior of apatite during crustal anatexis: Equilibrium and kinetic considerations. Geochimica et Cosmochimica Acta 48, 1464–1477.

Jayananda, M., Chardon, D., Peucat, J.J., Tushipokla, Fanning, C.M., 2015. Paleo- to Mesoarchean TTG accretion and continental growth in the western Dharwar craton, Southern India: Constraints from SHRIMP U–Pb zircon geochronology, whole-rock geochemistry and Nd–Sr isotopes. Precambrian Research 268, 295-322.

Jayananda, M., Gireesh, R.V., Sekhamo, K., Miyazaki, T., 2014. Coeval Felsic and Mafic Magmas in Neoarchean Calc-alkaline Magmatic Arcs, Dharwar Craton, Southern India: Field and Petrographic Evidence from Mafic to Hybrid Magmatic Enclaves and Synplutonic Mafic Dykes. Journal Geological Society of India 84, 5-28.

Jayananda, M., Moyen, J.-F., Martin, H., Peucat, J.-J., Auvray, B., Mahabaleshwar, B., 2000. Late Archaean (2550–2520 Ma) juvenile magmatism in the eastern Dharwar craton, southern India: constraints from geochronology, Nd–Sr isotopes and whole rock geochemistry. Precambrian Research 99, 225–254.

Jayananda, M., Tsutsumi, Y., Miyazaki, T., Gireesh, R. V., Kapfo, K., Tushipokla, Hadaka, H., Kano, T., 2013. Geochronological constraints on Meso- and Neoarchean regional metamorphism and magmatism in the Dharwar craton, southern India. Journal of Asian Earth Sciences 78(10), 18-38.

Jiang, H., Han, J., Chen, H., Zheng, Y., Lu, W., Deng, G., Tan, Z., 2017. Intra-continental back-arc basin inversion and Late Carboniferous magmatism in Eastern Tianshan, NW China: Constraints from the Shaquanzi magmatic suite. Geoscience Frontiers 8, 1447-1467.

Kumar, C.I., Windley, B.F., Horie, K., Kato, T., Hokada, T., Itaya, T., Yagi, K., Gouzu, C., Sajeev, K., 2013. A Rodinian suture in western India: New insights on India-

Madagascar correlations. Precambrian Research 236, 227-251.

Kumar, R.T.R., Santosh, M., Yang, Q.Y., Kumar, C.I., Chen, N.S., Sajeev, K., 2016. Archean tectonics and crustal evolution of the Biligiri Rangan Block, southern India. Precambrian Research 275, 406-428.

Lancaster, P.J., Dey, S., Storey, C.D., Mitra, A., Bhunia, R.K., 2015. Contrasting crustal evolution processes in the Dharwar craton: Insights from detrital zircon U–Pb and Hf isotopes. Gondwana Research 28, 1361-1372.

Li, S. S., Santosh, M., Cen, K., Teng, X. M., He, X. F., 2016. Neoarchean convergent margin tectonics associated with microblock amalgamation in the north china craton: evidence from the yishui complex. Gondwana Research 38, 113-131.

Liu, J., Wang, C., Liu, Y., Zhang, H., Ge, J., 2017. Middle Permian Wuhaolai mafic complex in the northern North China Craton: Constraints on the subduction‐related metasomatic mantle and tectonic implication. Geological Journal 1-19.

Loose, D., Schenk, V., 2018. 2.09 Ga old eclogites in the Eburnian-Transamazonian orogen of southern Cameroon: Significance for Palaeoproterozoic plate tectonics. Precambrian Research 304, 1-11.

Ma, X., Fan, H-R., Santosh, M., Guo, J., 2013. Geochemistry and zircon U–Pb chronology of charnockites in the Yinshan Block, North China Craton: tectonic evolution involving Neoarchaean ridge subduction. International Geology Review 55, 13, 1688-1704.

Maibam, B., Gerdes, A., Goswami, J.N., 2016. U–Pb and Hf isotope records in detrital and magmatic zircon from eastern and western Dharwar craton, southern India:

Evidence for coeval Archaean crustal evolution. Precambrian Research 275, 496-512.

Manikyamba, C., Said, N., Santosh, M., Saha, A., Ganguly, S., Subramanyam, K. S. V., 2017. U enrichment and Th/U fractionation in Archean boninites: implications for paleo-ocean oxygenation and U cycling at juvenile subduction zones. Journal of Asian Earth Sciences, https://doi.org/10.1016/j.jseaes.2017.10.009.

McLennan, S.M., Hemming, S., McDaniel, D.K., Hanson, G.N., 1993. Geochemical approaches to sedimentation, provenance, and tectonics. Geological Society of America Special Paper 284, 21–40.

Mclennan, S. M., 1989. Rare earth elements in sedimentary rocks: influence of provenance and sedimentary processes. Reviews in Mineralogy, 21(8), 169-200.

Moyen, J.F., Nédélec, A., Martin, H., Jayananda, M., 2001. Multi-element geochemical modelling of crust–mantle interactions during late-Archaean crustal growth: the Closepet granite (South India). Precambrian Research 112, 87-105.

Moyen, J.F., Nédélec, A., Martin, H., Jayananda, M., 2003. Syntectonic granite emplacement at different structural levels: the Closepet granite, South India. Journal of Structural Geology 25, 611-631.

Nance, R.D., Murphy, J.B., Santosh, M., 2014. The supercontinent cycle: a retrospective essay. Gondwana Research 25, 4–29.

Pearce, J.A., 2008. Geochemical fingerprinting of oceanic basalts with applications to ophiolite classification and the search for Archean oceanic crust. Lithos 100, 14-48.

Peucat, J. J., Jayananda, M., Chardon, D., Capdevila, R., Fanning, C. M., Paquette, J. L.,

2013. The lower crust of the Dharwar Craton, Southern India: Patchwork of Archean granulitic domains. Precambrian Research 227, 4-28.

Peucat, J. J., Mahabaleswar, B., Jayananda, M., 1993. Age of younger tonalitic magmatism and granulitic metamorphism in the South Indian transition zone (Krishnagiri area); comparison with older Peninsular gneisses from the Gorur–Hassan area. Journal of Metamorphic Geology 11(6), 879-888.

Rajesh, H.M., 2012. A geochemical perspective on charnockite magmatism in Peninsular India. Geoscience Frontiers 3, 773-788.

Rajesh, H.M., Chisonga, B.C., Shindo, K., Beukes, N.J., Armstrong, R.A., 2013. Petrographic, geochemical and SHRIMP U–Pb titanite age characterization of the Thabazimbi mafic sills: extended time frame and a unifying petrogenetic model for the Bushveld Large Igneous Province. Precambrian Research 230, 79–102.

Rajesh, H.M., Santosh, M., 2004. Charnockitic magmatism in southern India. Journal of Earth System Science 113, 565-585.

Rao, V.V., Murty, A.S.N., Dipankar, S., Bhaskar Rao, Y.J., Khare, P., Prasad, A.S.S.S.R.S., Sridher, V., Raju, S., Rao, G.S.P., Karuppannan, Kumar, N.P., Sen, M.K., 2015. Crustal velocity structure of the Neoarchean convergence zone between the eastern and western blocks of Dharwar Craton, India from seismic wide-angle studies. Precambrian Research 266, 282-295.

Rasmussen, B., Meier, D.B., Krapez, B., Muhling, J.R., 2013. Iron silicate microgranules as precursor sediments to 2.5-billion-year-old banded iron formations. Geology 41, 435-438.

Roberts, N. M. W. and Spencer, C.J., 2015. The zircon archive of continent formation through time. Geological Society London Special Publication 389, 197–225.

Ross, P.-S., Bedard, J.H., 2009. Magmatic affinity of modern and ancient sub-alkalinevolcanic rocks determined from trace element discriminant diagrams. Canadian Journal of Earth Sciences 46, 823–839.

Samuel, V. O., Santosh, M., Liu, S., Wang, W., Sajeev, K. 2014. Neoarchean continental growth through arc magmatism in the Nilgiri Block, southern India. Precambrian Research 245(1), 146-173.

Santosh, M., Arai, T., Maruyama, S., 2017. Hadean Earth and primordial continents: The cradle of prebiotic life. Geoscience Frontiers 8, 309-327.

Santosh, M., Li, S.S., 2018. Anorthosites from an Archean continental arc in the Dharwar Craton, southern India: implications for terrane assembly and cratonization. Precambrian Research, https://doi.org/10.1016/j.precamres.2018.02.011.

Santosh, M., Maruyama, S., Yamamoto, S., 2009. The making and breaking of supercontinents: some speculations based on superplumes, super downwelling and the role of tectosphere. Gondwana Research 15(3), 324-341.

Santosh, M., Yang, Q.Y., Shaji, E., Tsunogae, T., Mohan, M.R., Satyanarayanan, M., 2015. An exotic Mesoarchean microcontinent: The Coorg Block, southern India. Gondwana Research 27: 165-195.

Santosh, M., Yokoyama, K., Biju-Sekhar, S., Rogers, J.J.W., 2003. Multiple Tectonothermal Events in the Granulite Blocks of Southern India Revealed from EPMA Dating: Implications on the History of Supercontinents. Gondwana Research

6, 29-63.

Spencer, C.J., Yakymchuk, C., Ghaznavi, M., 2017. Visualising data distributions with kernel density estimation and reduced chi-squared statistic. Geoscience Frontiers 8, 1–6.

Sun, S.S., McDonough, W.F., 1989. Chemical and isotopic systematics of oceanic basalts: implications for mantle composition and processes. In: Saunders, A.D., Norry, M.J. (Eds.), Magmatism in Ocean Basins. Special Publication.Geological Society of London, vol.42 pp. 313-345.

Tetreault, J.L., Buiter, S.J.H., 2014. Future accreted terranes: a compilation of island arcs, oceanic plateaus, submarine ridges, seamounts, and continental fragments. Solid Earth Discuss 6, 1451-1521.

Thieblemont, D., Tegyey, M., 1994. Geochemical discrimination of differentiated magmatic rocks attesting for the variable origin and tectonic setting of calc-alkaline magmas. Comptes Rendus De Academie Des Sciences Series II 319, 87-94.

Tindle, A., G., Pearce, J., A., 1981. Petrogenetic modelling of in situ fractional crystallization in the zoned Loch Doon pluton Scotland. Contributions to Mineralogy and Petrology 78, 196–207.

Touret, J.L.R., Santosh, M., Huizenga, J.M., 2016. High temperature granulites and supercontinents. Geoscience Frontiers 7, 101-113.

Wilson, M., 1989. Igneous Petrogenesis. Unwin Hyman, London, p. 466.

Winchester, J.A., Floyd, P.A., 1977. Geochemical discrimination of different magma series and their differentiation products using immobile elements. Chem. Geol. 20,

325–343.

Woodhead, J. D., Hergt, J. M., Davidson, J. P., Eggins, S. M., 2001. Hafnium isotope evidence for 'conservative' element mobility during subduction zone processes. Earth Planetary Science Letters 192(3), 331-346.

Yang, Q. Y., Santosh, M., Ganguly, S., Arun-Gokul, J., Dev, S. G. D., Tsunogae, T., Shaji, E., Dong, Y.P., Manikyamba, C., 2016. Melt-fluid infiltration in Archean suprasubduction zone mantle wedge: evidence from geochemistry, zircon U–Pb geochronology and Lu–Hf isotopes from Wynad, southern India. Precambrian Research 281, 101-127.

Yang, Q.Y., Santosh, M., 2015. Zircon U–Pb geochronology and Lu–Hf isotopes from the Kolar greenstone belt, Dharwar Craton, India: Implications for crustal evolution in an ocean-trench-continent transect. Journal of Asian Earth Sciences 113, 797-811.

Yang, Q.Y., Santosh, M., Pradeepkumar, A.P., Shaji, E., Prasanth, R.S., Dhanil Dev, S.G., 2015. Crustal evolution in the western margin of the Nilgiri Block, southern India: Insights from zircon U–Pb and Lu–Hf data on Neoarchean magmatic suite. Journal of Asian Earth Sciences 113, 766-777.

Yano, M., Tsunogae, T., Santosh, M., Yang, Q.Y., Shaji, E., Takamura, Y., 2016. Ultrahigh-temperature metagabbros from Wynad: Implications for Paleoproterozoic hot orogen in the Moyar Suture Zone, southern India. Journal of Asian Earth Sciences 130, 139-154.

Zhai, M.G., Santosh, M., 2011. The early Precambrian odyssey of the North China Craton: a synoptic overview. Gondwana Research 20, 6–25.

Zhao, J.J., Zhou, M.F., 2007. Geochemistry of Neoproterozoic mafic intrusions in the Panzhihua district (Sichuan Province, SW China): implications for subduction related metasomatism in the upper mantle. Precambrian Research 152, 27-47.

Zhu, M., Dai, Y., Zhang, L.,Wang, C., Liu, L., 2015. Geochronology and geochemistry of the Nanfen iron deposit in the Anshan–Benxi area, North China Craton: implications for ~2.55 Ga crustal growth and the genesis of high-grade iron ores. Precambrian Research 260, 23–38.

Figure captions

Fig. 1 Geological frame work of the Dharwar Craton in the southern India (after Kumar et al., 2016), and this study area showing the Nallamalai Suture Zone. Abbreviations: ChSZ—Chitradurga Shear Zone, KolSZ— Kolar Suture Zone; McSZ—Mercara Shear zone; SSZ— Salem Suture Zone; KoSZ—Kollegal Shear Zone; MeSZ—Mettur Shear Zone, NLSZ—Nallamalai Shear Zone, MSZ—Moyar Shear Zone, SASZ—Salem-Attur Shear Zone; BSZ—Bhavani Shear Zone, CaSZ—Cauvery Shear Zone, PCSZ—Palghat-Cauvery Shear Zone; KKPTSZ—Karur-Kambam-Painavu—Trichur Shear Zone; ASZ—Achankovil Shear Zone; WDC—Western Dharwar Craton; CDC—Central Dharwar Craton; EDC—Eastern Dharwar Craton; EGMB—Eastern Ghats Mobile Belts; KB—Karwar Block; CB—Coorg Block; BRB—Billigiri Rangan

Block; SB—Shevaroy Block; MdB—Madras Block; NB—Nilgiri Block; NkB—Namakkal Block; MB—Madurai Block; TB—Trivandrum Block.

Fig. 2 Geological map of the Nallamalai Suture Zone showing sample locations (after Geological Survey of India, 1987).

Fig. 3 Representative field photographs of the Nillamalai Suture Zone. **(A)** Coarse to medium grained charnockite with diorite enclave (NM-2-1, NM-2-2); **(B)** foliated granodiorite (NM-3-1); **(C)** pink granite (NM-4-1); **(D)** large exposure of amphibolite migmatised with **(E)** hornblende gneiss and pink granite (NM-5-1, NM-5-2, NM-5-3); **(F)** meta-monzogranite with amphibolite enclave (NM-8-1, NM-8-2).

Fig. 4 Representative field photographs of the Nillamalai Suture Zone. **(A)** Coarse to medium grained Grt-charnockite (NM-11-1); **(B)** and **(C)** layered and metamorphosed BIF with mesoscopic scale folding (NM-14-1, NM-14-2); **(D)** large exposure of fractured BIF (NM-15-1); **(E)** BMQ with fine millimeters quartz veins (NM-14-3, NM-14-4); **(F)** Grt-charnockite showing as foliated layers (NM-16-2).

Fig. 5 Representative photomicrographs of the Nillamalai Suture Zone. **(A)** Charnockite showing K-feldspar, plagioclase, quartz, orthpopyroxene, biotite,

magnetite assemblage (NM-2-1); **(B)** Clinopyroxene, hornblende, quartz, orthopyroxene and plagioclase assemblage in diorite (NM-2-2); **(C)** K-feldspar, plagioclase, quartz, hornblende, biotite, magnetite in granodiorite (NM-3-1); **(D)** K-feldspar, plagioclase, quartz, biotite, magnetite assemblage in granite (NM-4-1); **(E)** K-feldspar, plagioclase, quartz, clinopyroxene, orthopyroxene, garnet, biotite assemblage in Grt-charnockite (NM-11-1); **(F)** K-feldspar, plagioclase, quartz, orthopyroxene assemblage in charnockite (NM-13-1); **(G)** K-feldspar, quartz, epidote and zoisite assemblage in granitic pegmatite (NM-16-1); **(H)** K-feldspar, plagioclase, garnet, quartz, biotite, hypersthene, magnetite assemblage in Grt-charnockite (NM-16-2); **(I)** plagioclase, clinopyroxene, garnet, biotite, magnetite assemblage in Grt-Bt gneiss (NM-17-1). Mineral abbreviations: Pl-plagioclase, Kfs- K-feldspar; Qtz- quartz; Cpx-clinopyroxene, Opx-orthopyroxene; Hbl-hornblende; Bt-biotite, Grt- garnet; Hy-hypersthene; Mic- microcline; Mt-magnetite; Ep-epidote; Zo-zoisite; Zr-zircon; Ttn-titanite; Ap-apatite.

Fig. 6 Representative photomicrographs of the Nillamalai Suture Zone. **(A)**, **(B)** and **(C)** Banded iron formation showing magnetite, quartz, orthopyroxene assemblage (NM-14-2); **(D)** and **(E)** magnetite, quartz, clinopyroxene assemblage in BIF (NM-14-1); **(F)** and **(G)** orthopyroxene , clinopyroxene, hornblende, magnetite, quartz assemblage in BMQ (NM-14-3); **(H)** and **(I)** orthopyroxene , hornblende, magnetite, quartz assemblage in BIF (NM-15-1).

Mineral abbreviations: Cpx-clinopyroxene, Opx-orthopyroxene; Hbl-hornblende; Qtz- quartz; Mt-magnetite.

Fig. 7 (A) Nb/Y vs. Zr/TiO_2 geochemical classification diagram (after Winchester and Floyd, 1977) showing the basaltic to rhyodacitic compositional spectrum of precursor magmas for the mafic-intermediate-felsic association from NLSZ. **(B)** Zr vs. Y plot (after Ross and Bedard, 2009) reflecting tholeiitic to calc-alkaline character for amphibolite-diorite-granodiorite assemblage from NLSZ.

Fig. 8 Primitive mantle normalized trace element abundance patterns and chondrite-normalized REE patterns (normalization values are from Sun and McDonough, 1989) for amphibolite, diorite-granodiorite, charnockite, garnet-biotite gneiss, PASS-normalized REE patterns for BIF and BMQ (normalization values are from McLennan, 1989) from NLSZ.

Fig. 9 (A) Total alkali vs. silica diagram in which the studied charnockites plot in the fields for granite, granodiorite and syenodiorite, while the gneisses correspond to the fields for granite, syenodiorite and syenite (after Cox et al., 1979, and adapted from Wilson, 1989). **(B)** $CaO-Na_2O-K_2O$ triangular diagram reflecting granodiorite to quartz monzonite composition for charnockites and gneisses from NLSZ. **(C)** A=Al(Na+K+2Ca) vs. B=Fe+Mg+Ti plots showing low peraluminous, felsic source for the generation of charnockites and gneisses of NLSZ. **(D)** $Na_2O+K_2O–CaO$ vs. SiO_2 diagram

depicting the calc-alkalic to alkalic character of charnockites and alkali-calcic to alkali character of gneisses (Frost et al., 2001).

Fig.10 (A) $FeO^{(t)}/(FeO^{(t)} + MgO)$ vs. SiO_2 diagram (after Frost et al., 2001) showing the magnesian character of NLSZ charnockites and gneisses. **(B)** Sr–Rb–Ba triangular diagram (after Rajesh and Santosh, 2004) showing the plots for charnockites and gneisses in the field of high Ba-Sr granitoids. **(C)** Plot of Y vs. Sr/Y compositions for charnockites and gneisses from NLSZ suggesting their arc affinity and inputs from slab melting. The fields are from Drummond and Defant (1990). **(D)** Nb/Zr vs. Zr plot. with fields from Thieblemont and Tegyey (1994) showing subduction-collision tectonic regime for the emplacement of NLSZ charnockites and gneisses. **(E)** Rb-Hf-Ta tectonic discrimination diagram (after Tindle and Pearce, 1981) for NLSZ charnockite and gneisses attesting to volcanic arc related tectonic setting.

Fig. 11 (A) TiO_2 vs. SiO_2 and **(B)** P_2O_5 vs. SiO_2 plots for the NLSZ charnockite samples. The isotherms in (A) show Fe–Ti oxide saturation temperatures at 7.5 kbar (Green and Pearson, 1986), whereas those in (B) illustrate apatite saturation temperatures at 7.5 kbar (Harrison and Watson 1984).

Fig. 12 (A) Th/Yb vs. Nb/Yb plots (after Pearce, 2008) showing active continental margin affinity for the mafic-intermediate-felsic association from NLSZ corroborating ocean-continent convergence and contributions of

subduction components towards generation of precursor magmas. Abbreviations: CA-calc-alkaline; TH-tholeiitic; SHO-shoshonite. **(B)** Zr/Nb vs. Nb/Th plot (after, Condie, 2005) with the studied samples corresponding to the arc field. **(C)** Nb/Zr vs. Th/Zr diagram (after Zhao and Zhou, 2007) showing the studied samples in an array consistent with fluid-related enrichment of mantle through subduction process. **(D)** Dy/Yb vs La/Yb diagram (after Rajesh et al., 2013) suggesting low degree partial melting of mantle in garnet peridotite regime for NLSZ samples.

Fig. 13 (A) SiO_2 vs. Al_2O_3 diagram (after Zhu et al., 2015) showing submarine hydrothermal affinity for the BIF and BMQ samples of NLSZ and suggesting their deposition in an oceanic realm associated with an active continental margin. **(B)** Th/U vs. Th plot showing that most of the BIF and BMQ samples are devoid of weathering (after McLennan et al., 1993). **(C**) Sm/Yb vs. Eu/Sm plot (after Alibo and Nozaki, 1999) suggesting deposition of studied BIFs from paleo-seawater with input from hydrothermal fluids.

Fig. 14 Representative Cathodoluminescence (CL) images of zircon grains from **(A)** meta-monzogranite (NM-8-1), **(B)** charnockite (NM-2-1), **(C)** diorite (NM-2-2), **(D)** amphibolite, **(E)** granodiorite (NM3-1), **(F)** Grt-charnockite (NM-16-2), **(G)** BIF (NM-14-1), **(H)** BMQ (NM-14-3), **(I)** BIF (NM-14-2), **(J)** granitic pegmatite (NM-16-1). Zircon U-Pb ages (Ma) and εHf(t) values are also

shown. The smaller white and black circles indicate spots of LA-ICP-MS U-Pb dating, whereas the larger yellow circles represent locations of Hf isotopic analyses.

Fig. 15 Wetherill U-Pb concordia plots and weighted average plots: **(A)** magmatic and **(B)** metamorphic age for NM-8-1; **(C)** magmatic and **(D)** metamorphic age for NM-5-1; **(E)** magmatic and **(F)** metamorphic age for NM-3-1. All data point uncertainties are 2σ, and the weighted mean ages bar width is the same as the uncertainties and include systematic error. The two different uncertainty values shown represent the cases without and with the systematic error propagated uncertainties incorporated for the weighted mean age, respectively.

Fig. 16 Wetherill U-Pb concordia plots and weighted average plots: **(A)** magmatic and **(B)** metamorphic age for NM-2-1; **(C)** magmatic and **(D)** metamorphic age for NM-2-2; **(E)** magmatic age for NM-16-1. All data point uncertainties are 2σ, and the weighted mean ages bar width is the same as the uncertainties and include systematic error. The two different uncertainty values shown represent the cases without and with the systematic error propagated uncertainties incorporated for the weighted mean age, respectively.

Fig. 17 Wetherill U-Pb concordia plots and weighted average plots: **(A)** magmatic and **(B)** metamorphic age for NM-16-2; **(C)** metamorphic age for NM-14-1; **(D)** metamorphic age for NM-14-2; **(E)** magmatic and **(F)** metamorphic age for NM-14-3. All data point uncertainties are 2σ, and the weighted mean ages bar width is the same as the uncertainties and include systematic error. The two different uncertainty values shown represent the cases without and with the systematic error propagated uncertainties incorporated for the weighted mean age, respectively.

Fig. 18 Chondrite-normalized REE diagrams. **(A)** sample NM-8-1, **(B)** NM-5-1, **(C)** NM-3-1, **(D)** NM-2-1, **(E)** NM-2-2, **(F)** NM-16-1. The red lines are from magmatic grains and blue lines are from metamorphic grains, chondrite values are after Sun and McDonough (1989).

Fig. 19 Chondrite-normalized REE diagrams. **(A)** sample NM-16-2, **(B)** NM-14-1, (**C**) NM-14-2, (**D**) NM-14-3. The red lines are from magmatic grains and blue lines are from metamorphic grains, chondrite values are after Sun and McDonough (1989). (**E**) U/Yb versus Y and (**F**) U versus Yb, the fields for continental or MORB source are from Grimes et al., 2007.

Fig. 20 Measured Lu-Hf isotopic data, error bars represent 2σ uncertainties. (**A**) $^{176}Lu/^{177}Hf$ versus $^{176}Hf/^{177}Hf$, (**B**) $^{176}Hf/^{177}Hf_i$ versus $^{206}Pb/^{207}Pb$ age, (**C**)

εHf(t) versus $^{206}Pb/^{207}Pb$ age, new crust line are after Dhuime et al., (2011). Crustal model ages T_{DM}^{C} were calculated using representative bulk crustal value $^{176}Lu/^{177}Hf$ =0.015 (Griffin et al., 2002).

Fig. 21 (**A**) Kernel density plot of combined zircon U-Pb data from this study the red colors represent magmatic age and blue is from metamorphic grains, (**B**) U versus $^{206}Pb/^{207}Pb$ age plot.

Fig. 22 Compilation of available Lu-Hf isotope data from south India, Coorg Block (Santosh et al., 2015), Biligiri Rangan Block (Kumar et al., 2016), Nilgiri Block (Yang et al., 2015), Wynad region (Yano et al., 2016), Kolar greenstone belt (Yang and Santosh, 2015), combined with data from this study.

Fig. 23 Combined age data shown as kernel density plots (following Spencer et al., 2017) from Dharwar Craton including: Shevaroy Block (Glorie et al., 2014; Clark et al., 2009; Peucat et al., 1993, 2013), Madras Block (Glorie et al., 2014; Crawford, 1969; Bernard-Griffiths et al., 1987), Kolar greenstone belt (Yang and Santosh, 2015; Balakrishnan et al., 1999), Biligiri Block (Peucat et al., 2013; Kumar et al., 2016), Niligiri Block (Peucat et al., 2013; Samuel et al., 2014; Yang et al., 2015), Eastern and Western Dharwar (Jayananda et al., 2013), Wynad region (Yano et al., 2016), together with this study.

Table captions

Table 1 Sample numbers, rock types, localities, GPS reading of samples from Nallamalai Suture Zone.

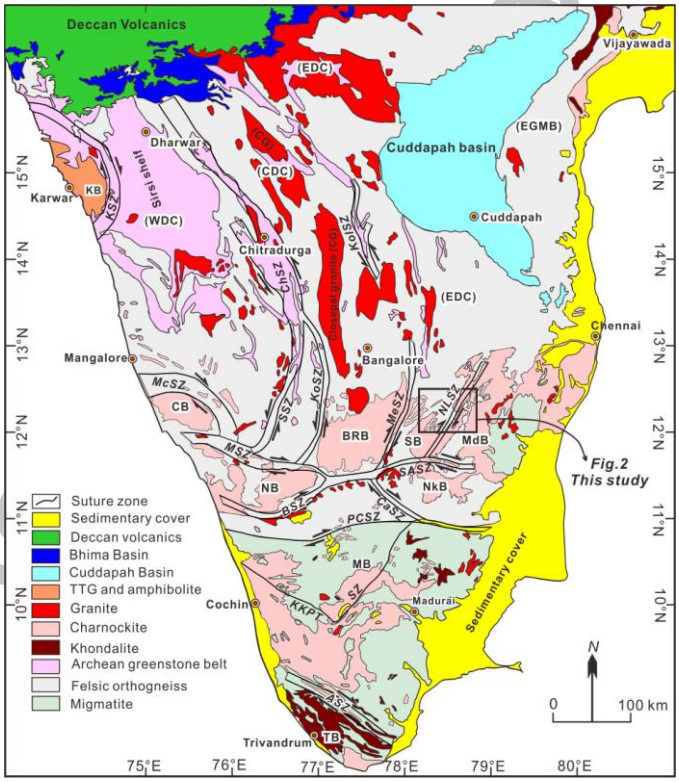

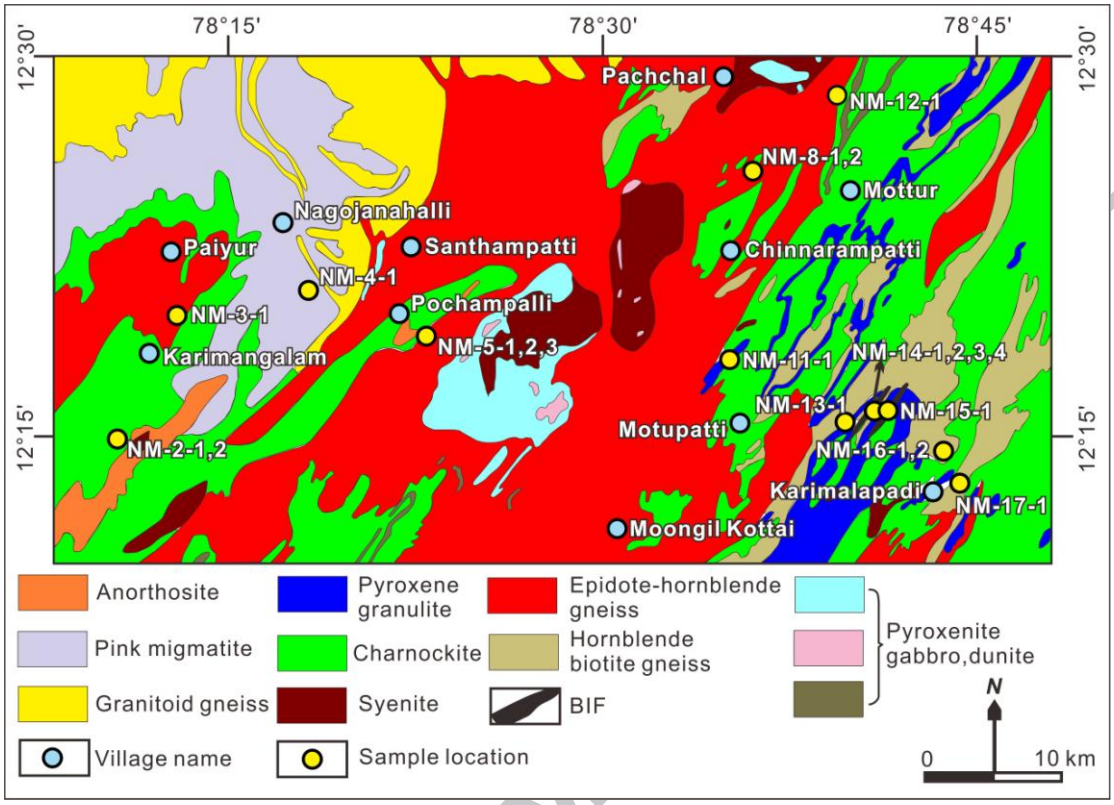

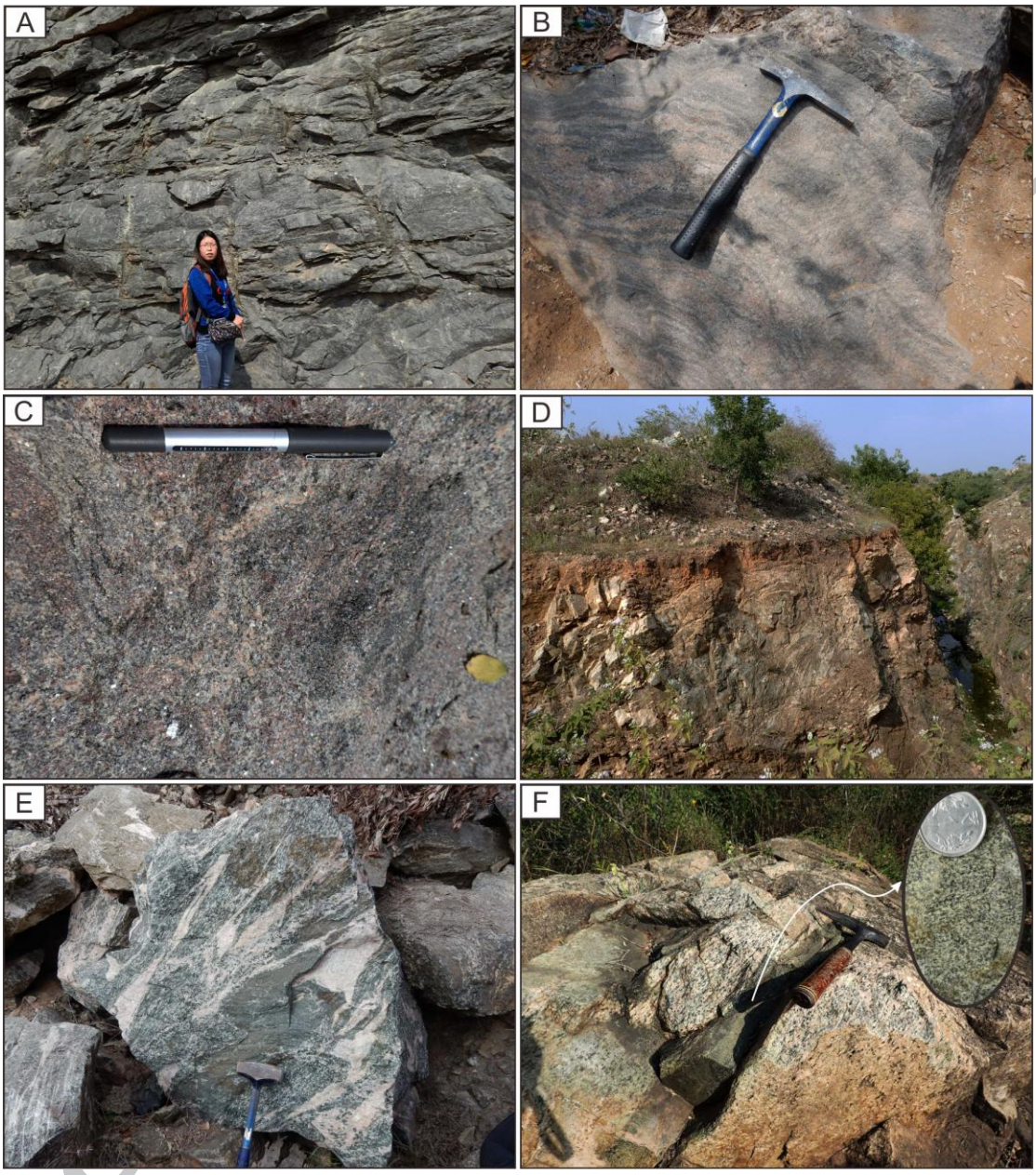

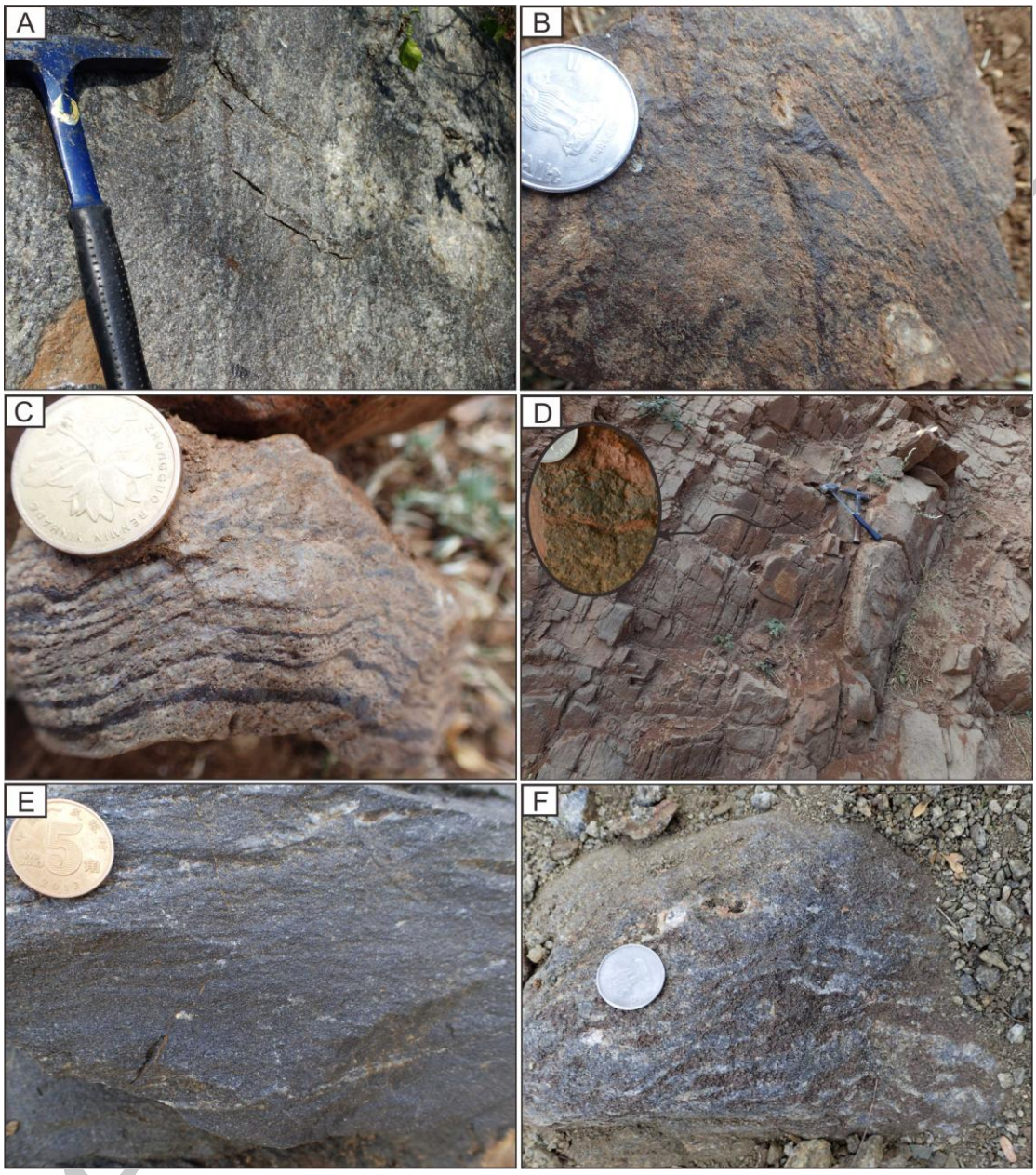

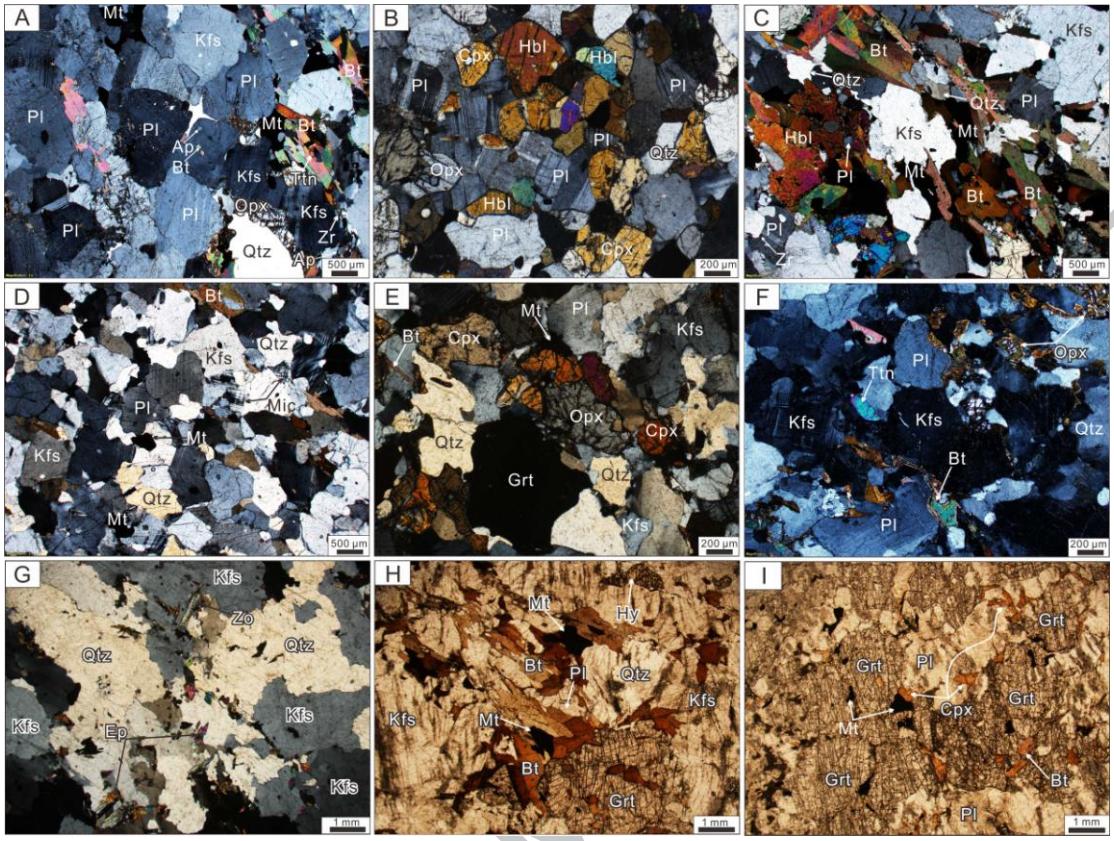

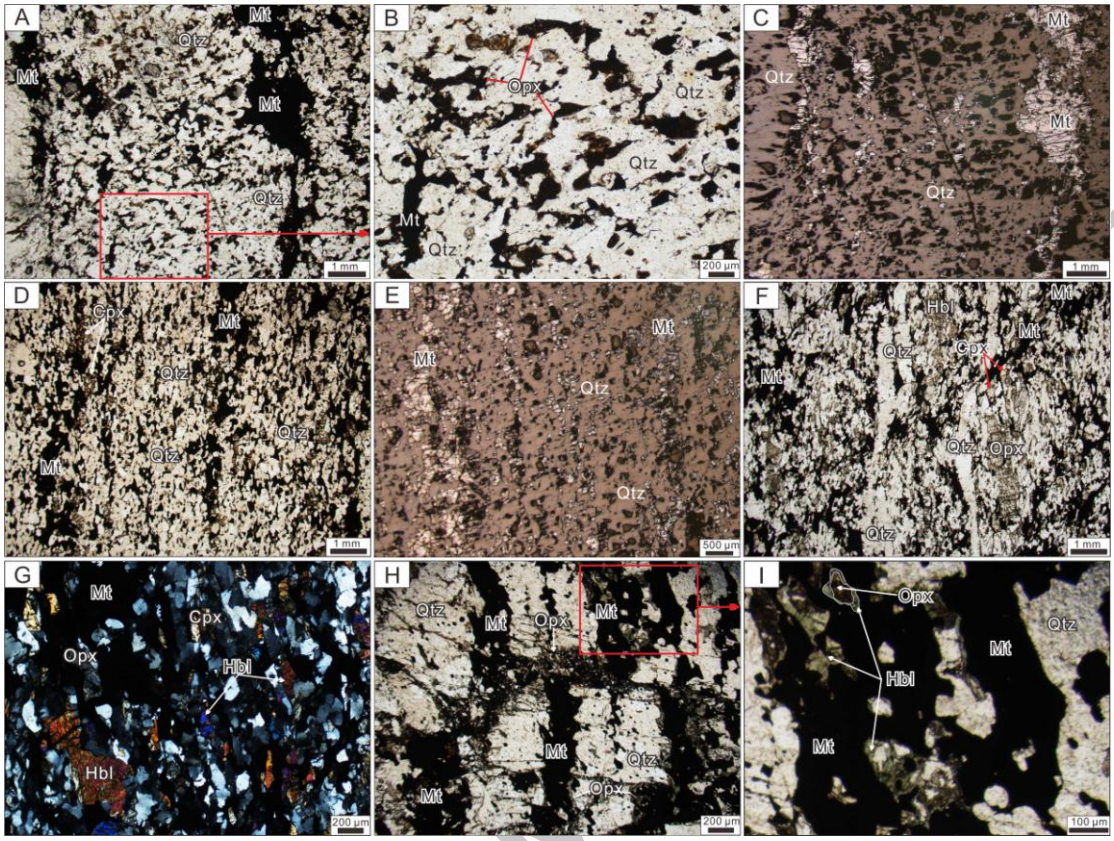

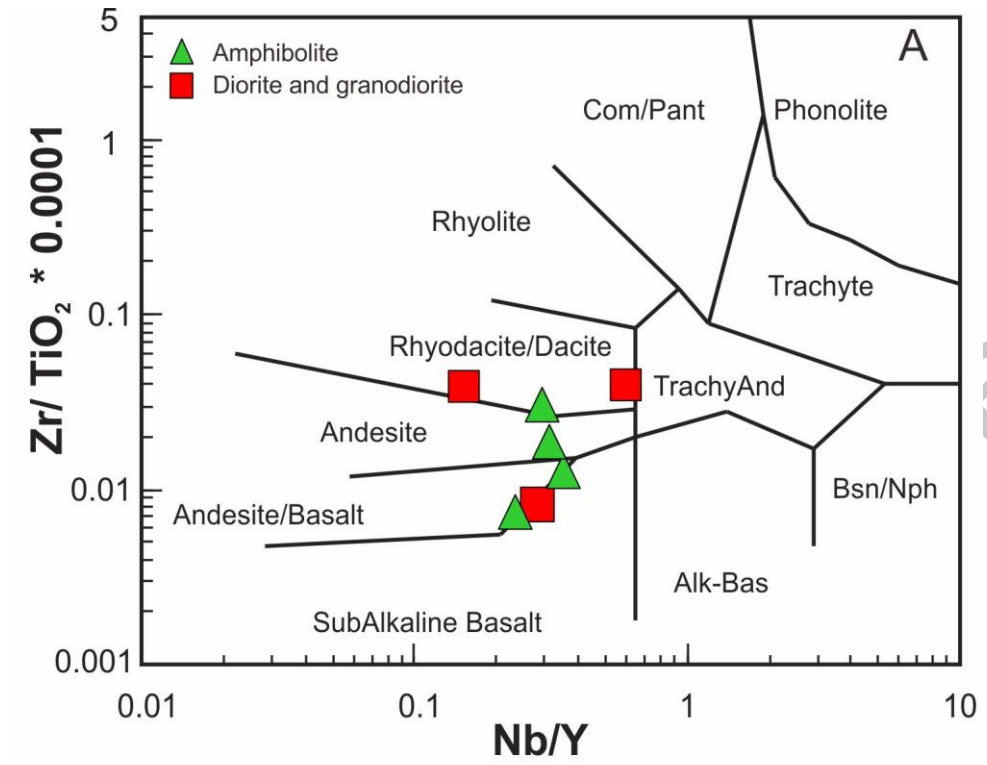

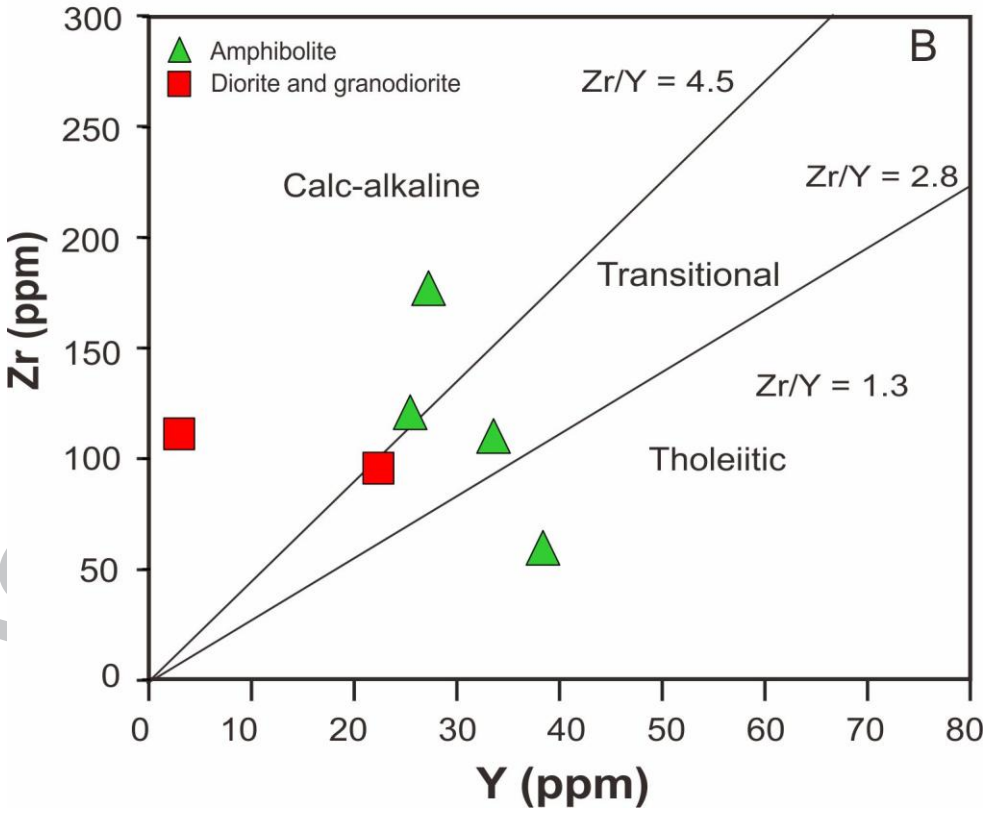

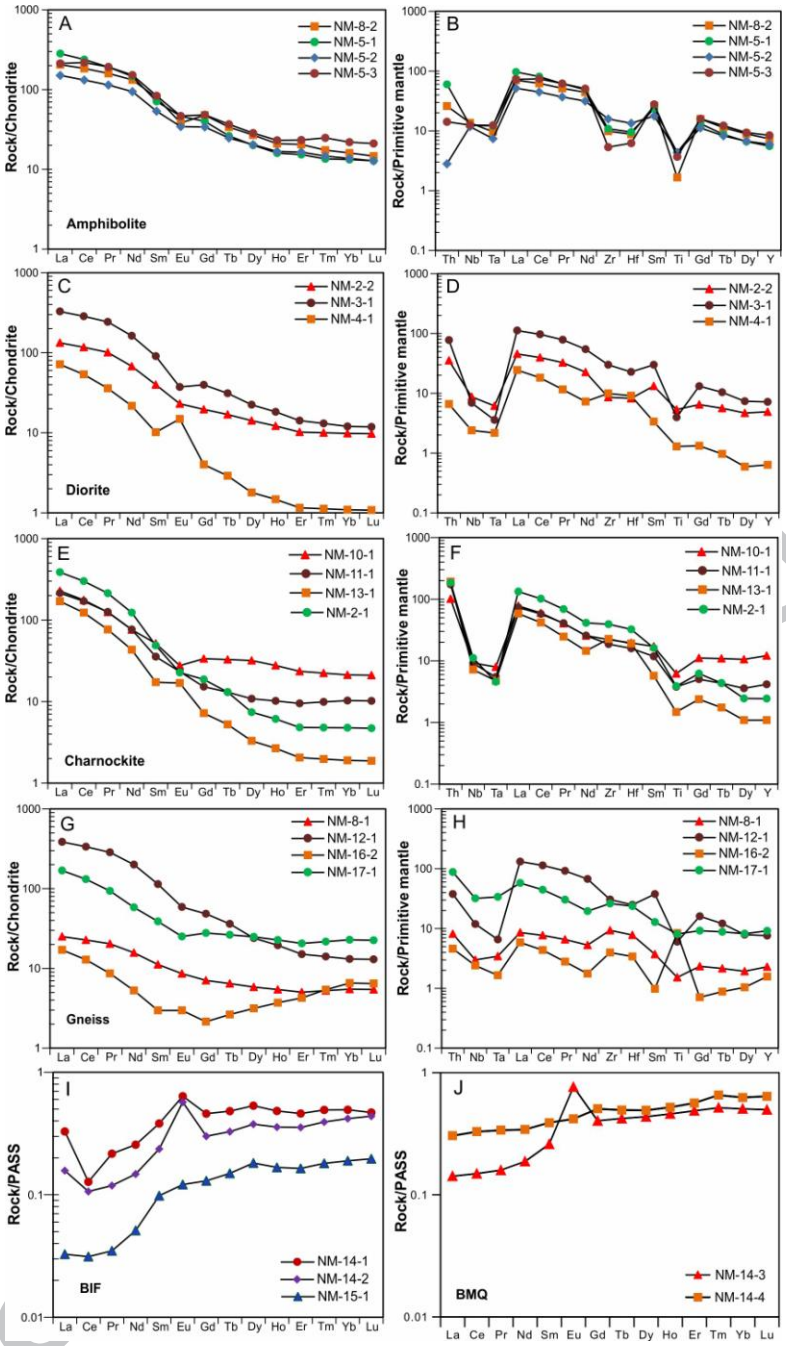

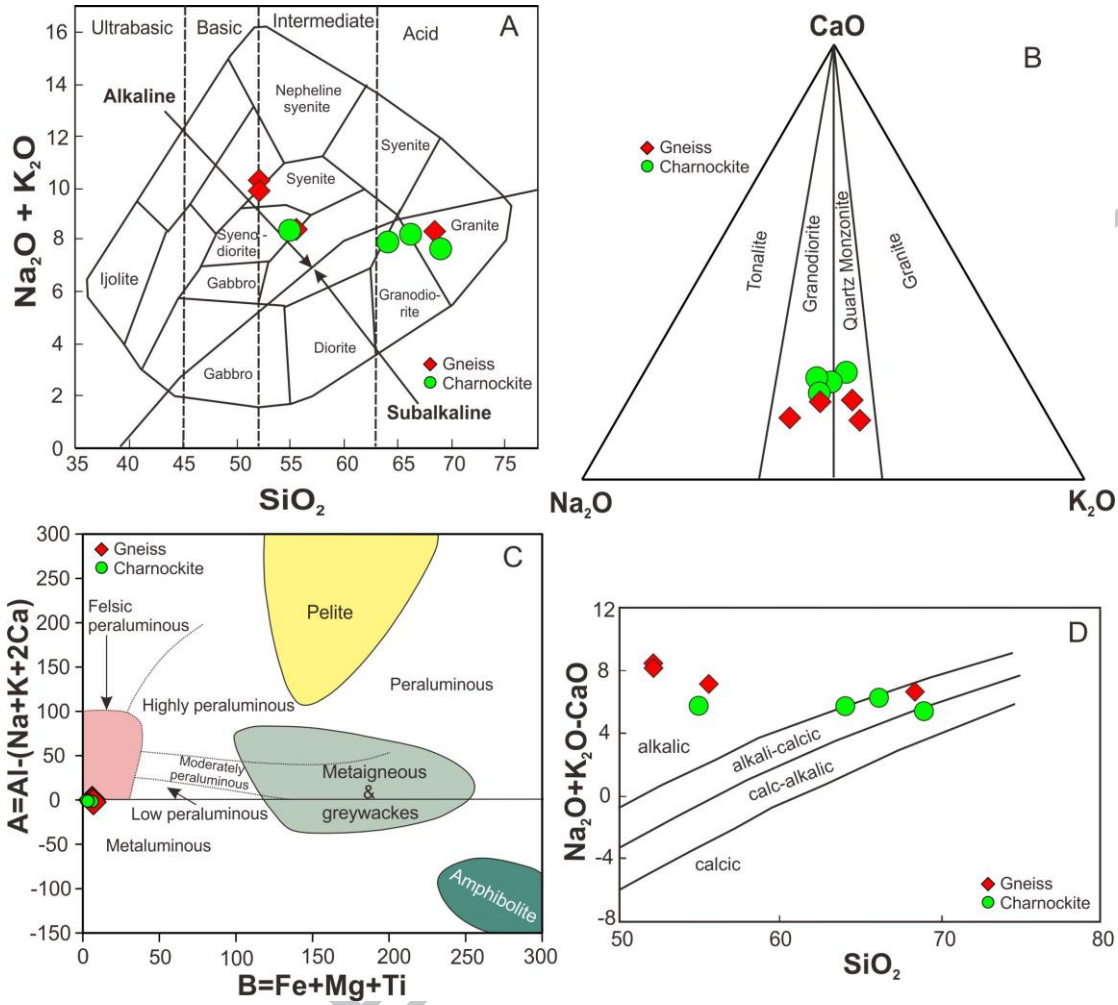

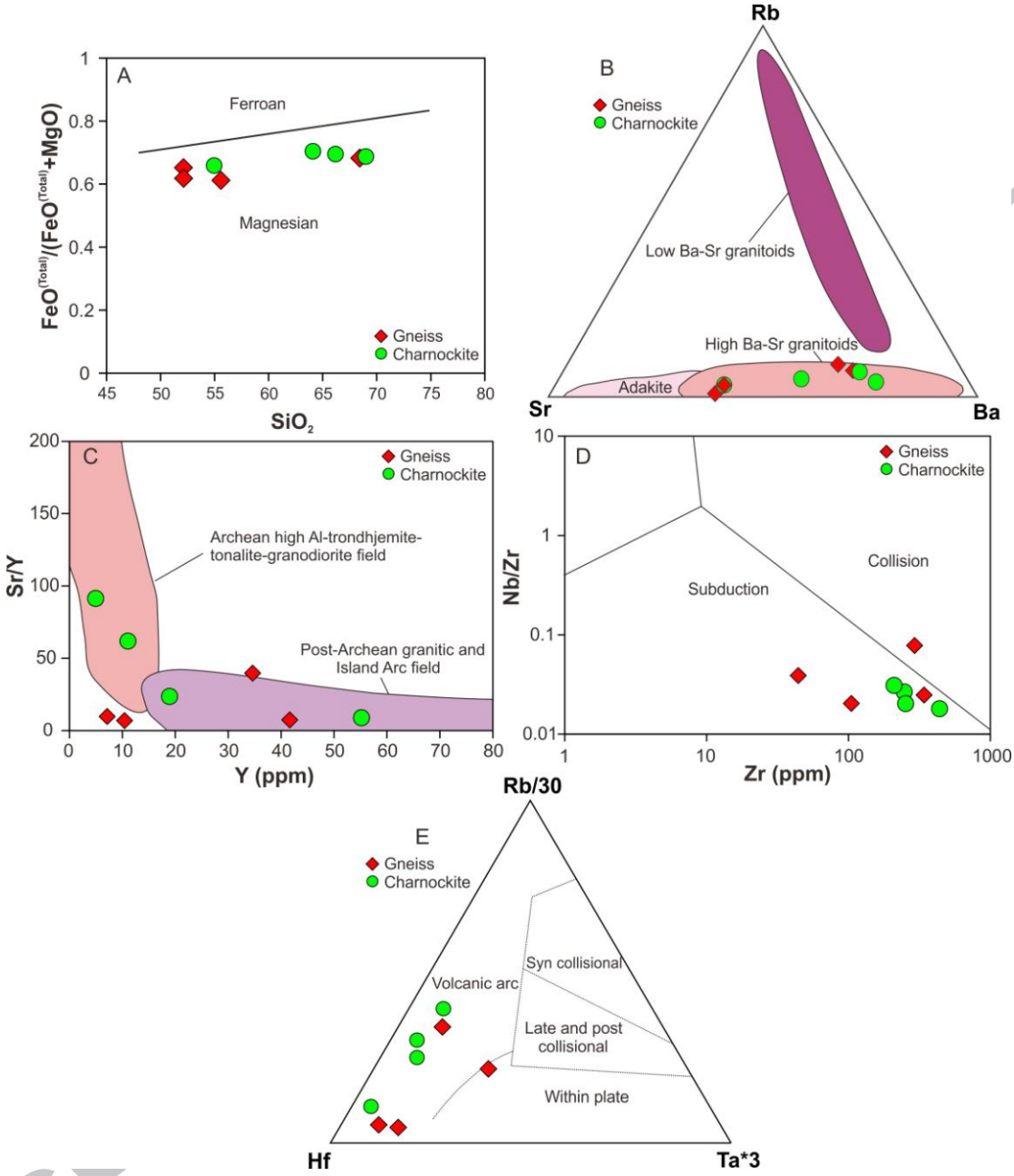

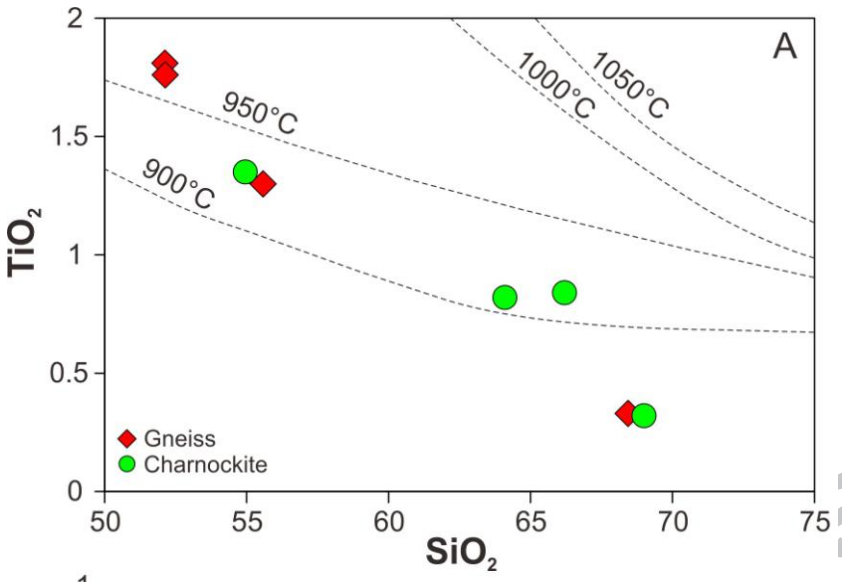

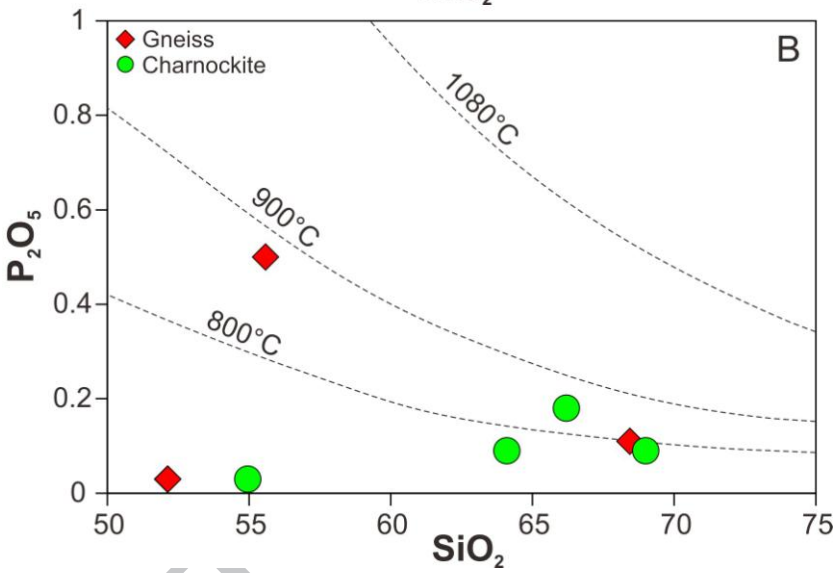

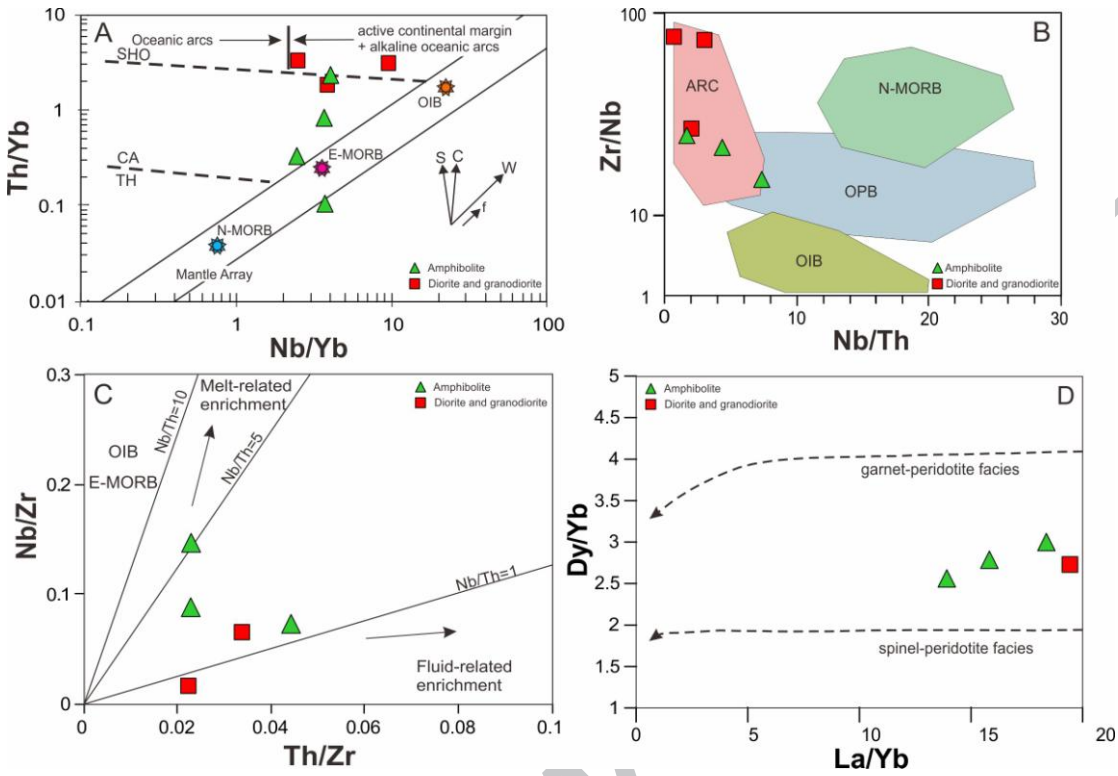

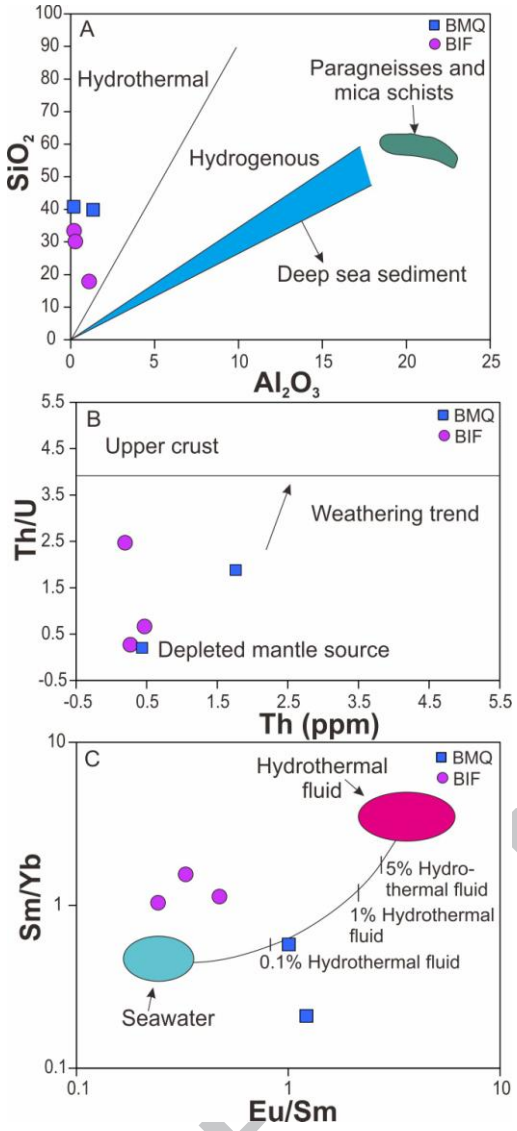

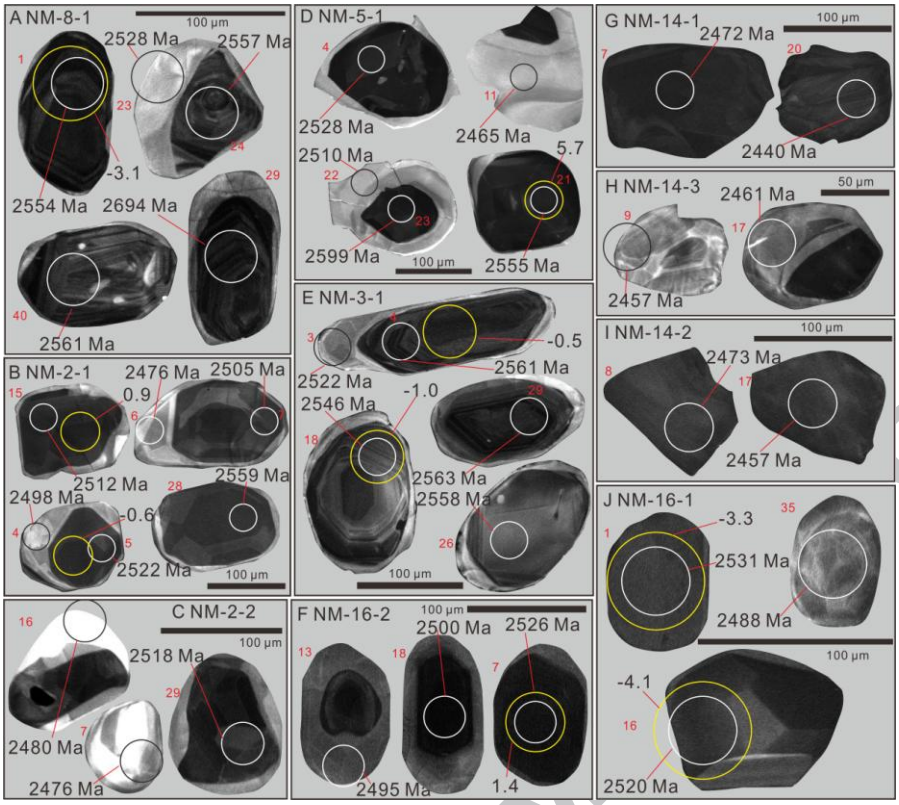

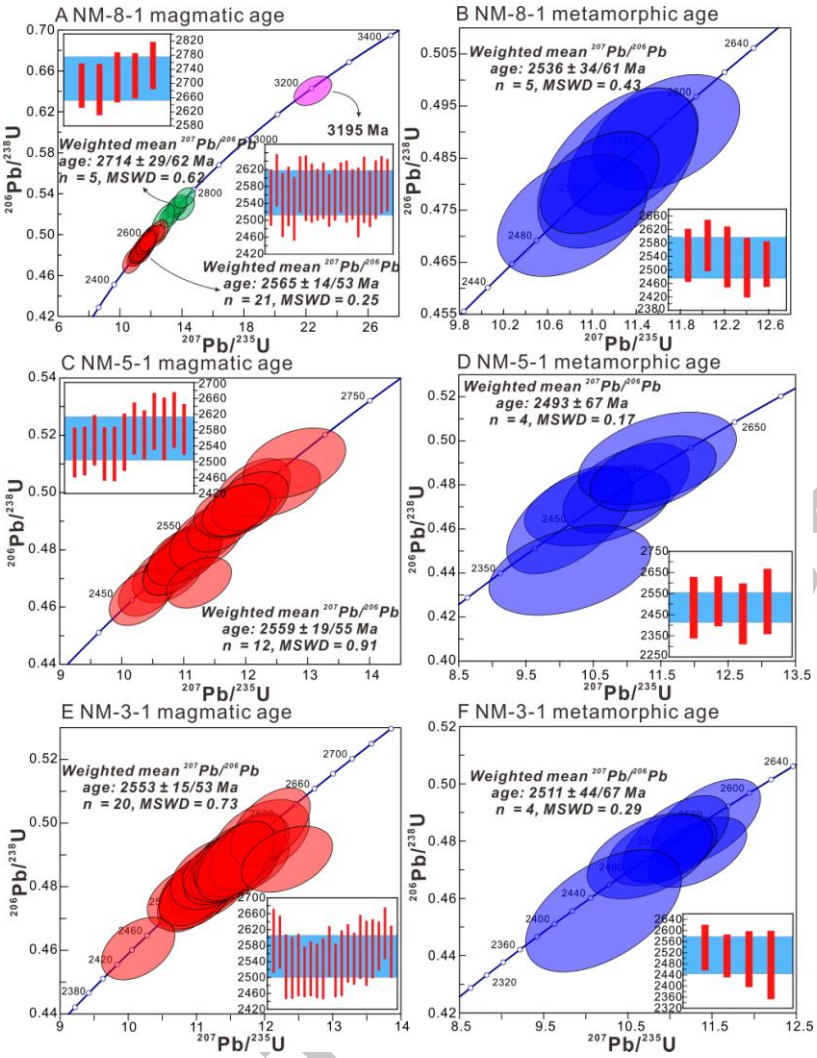

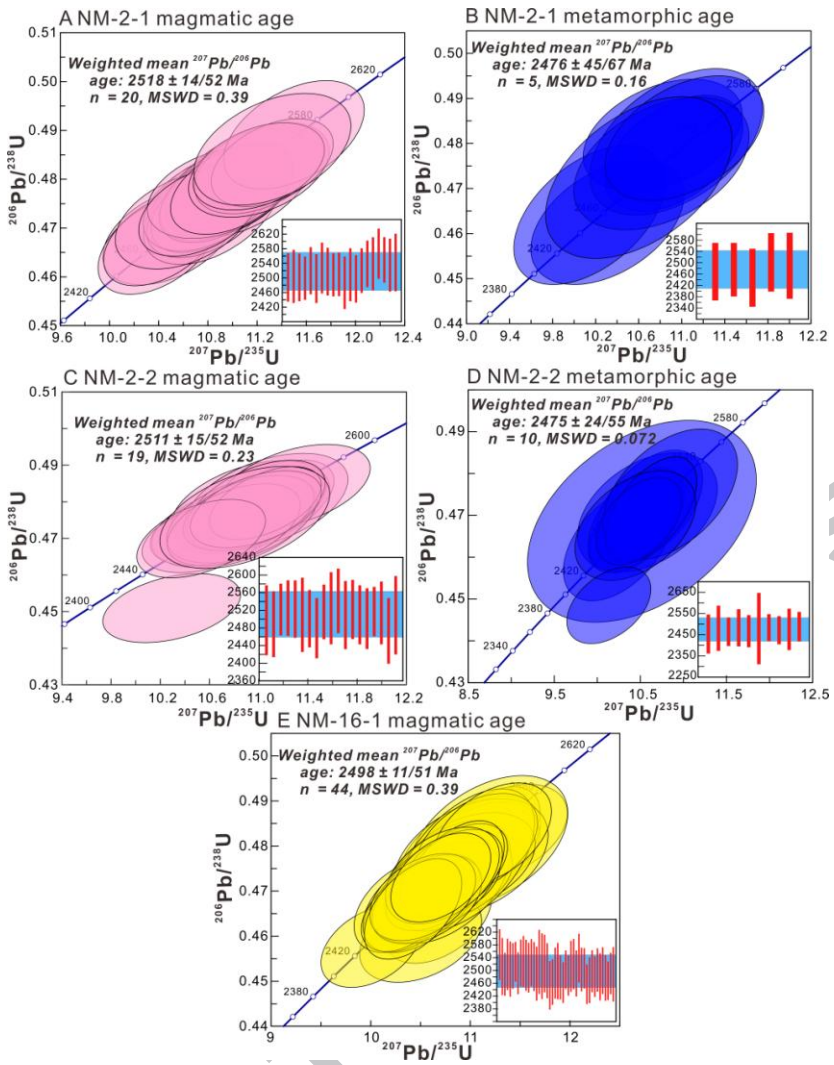

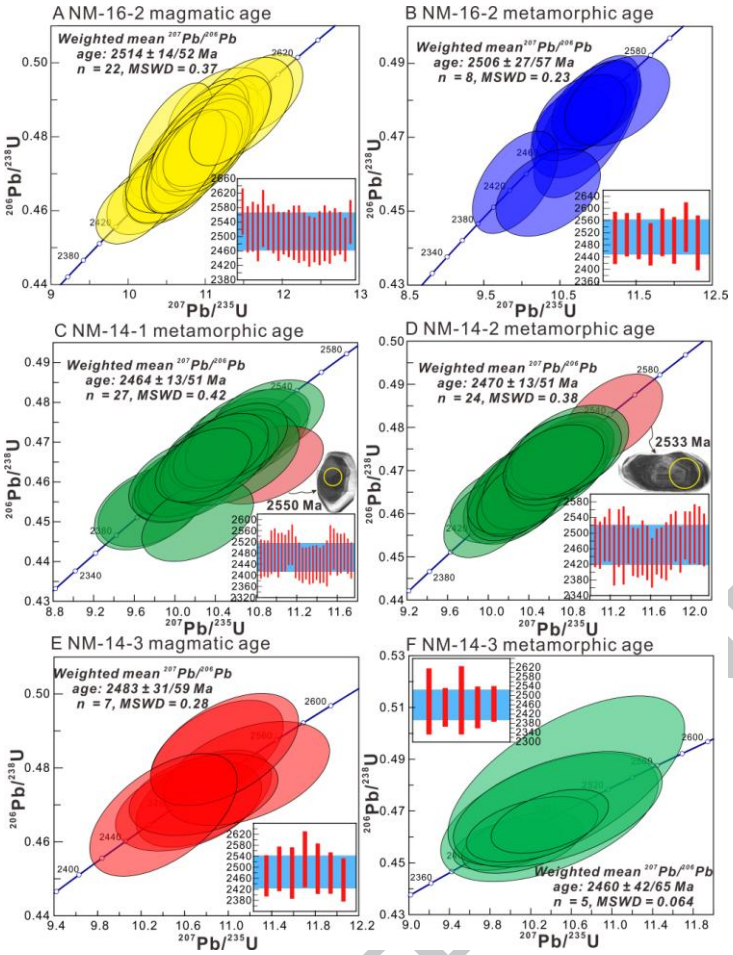

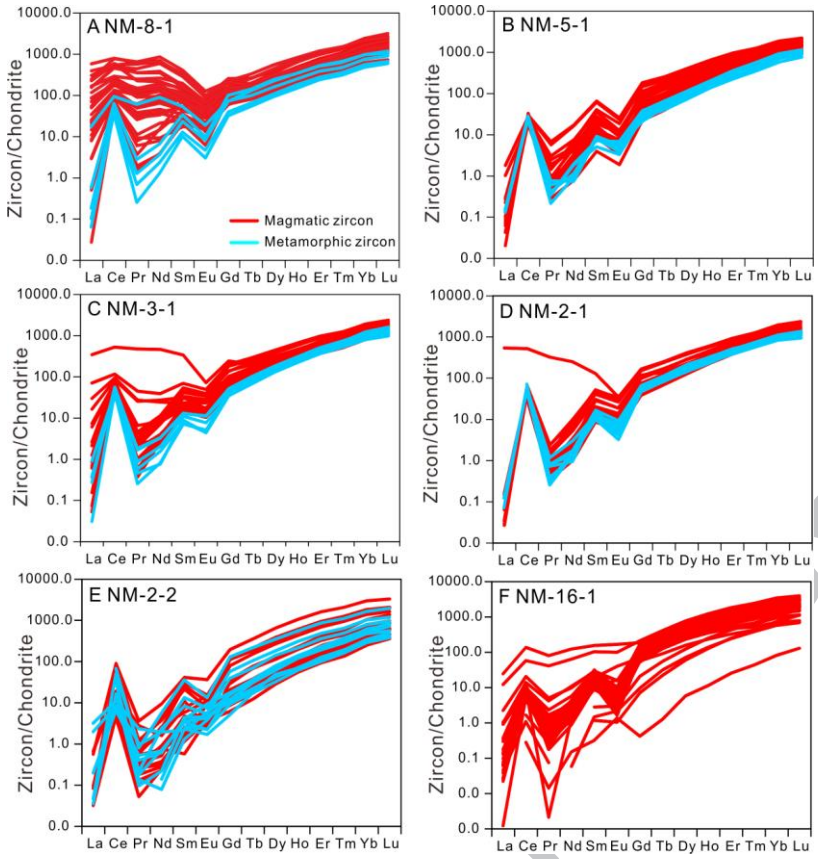

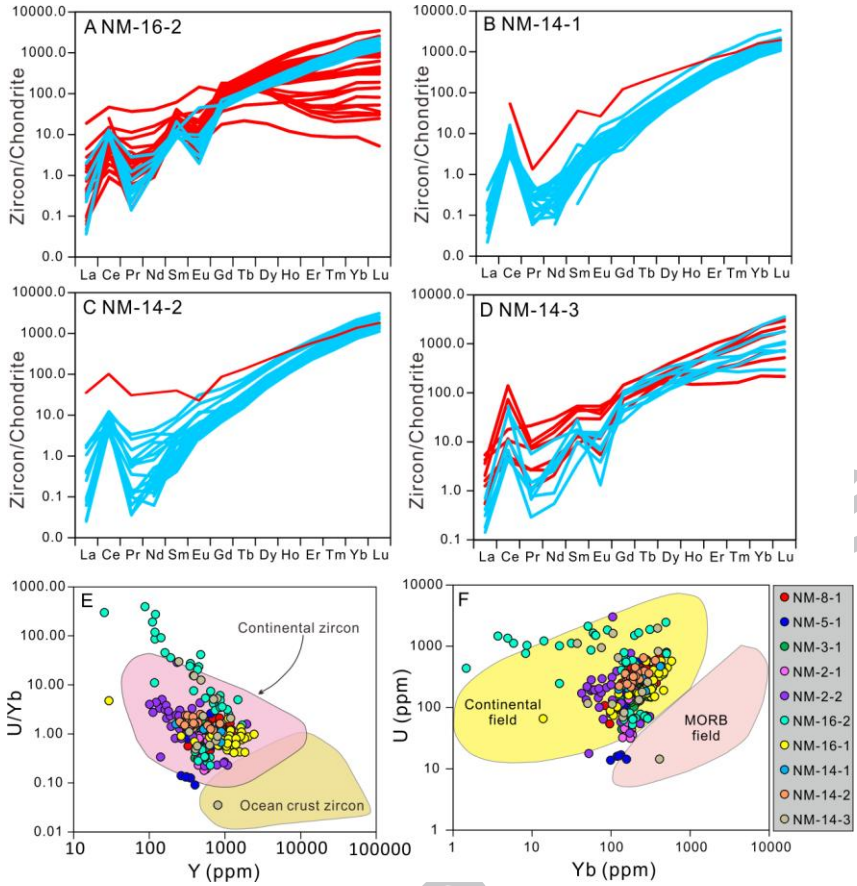

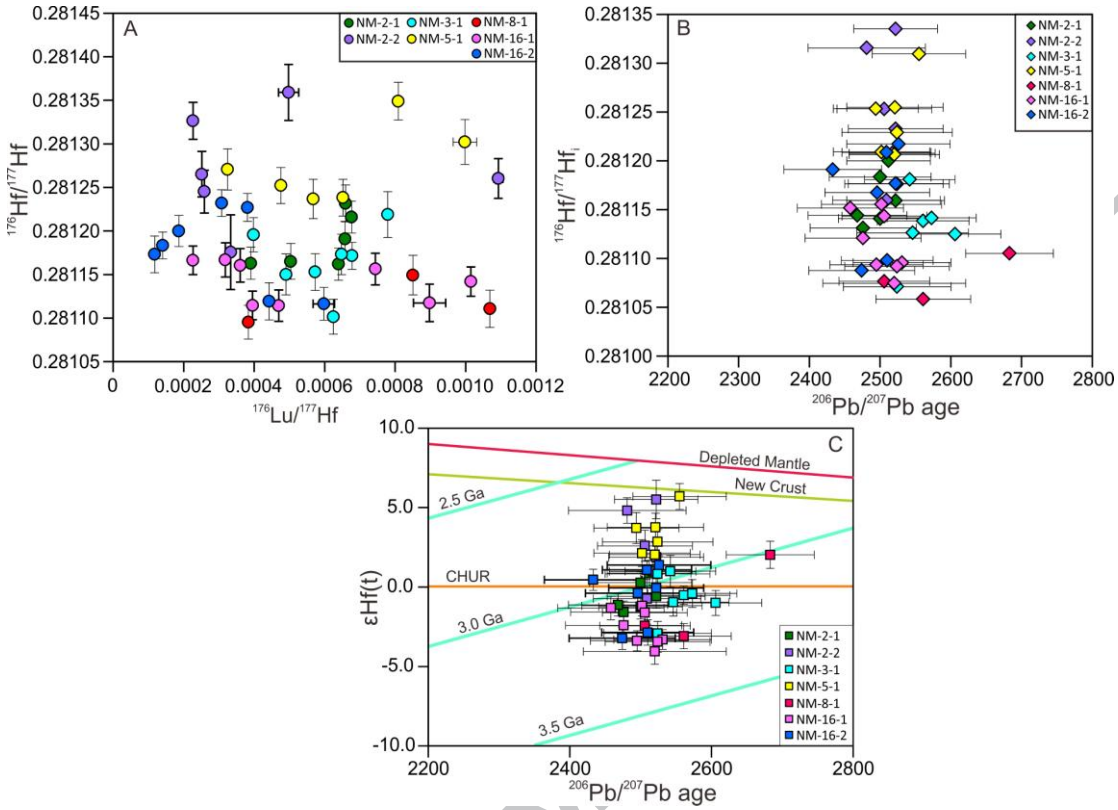

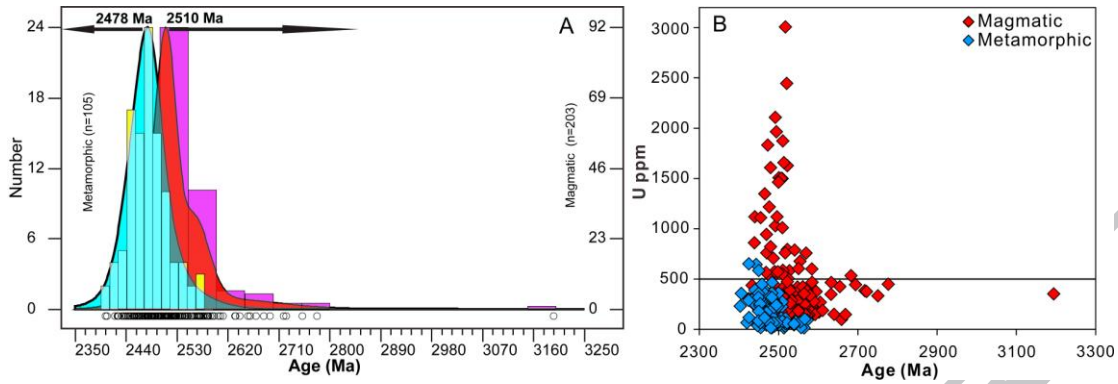

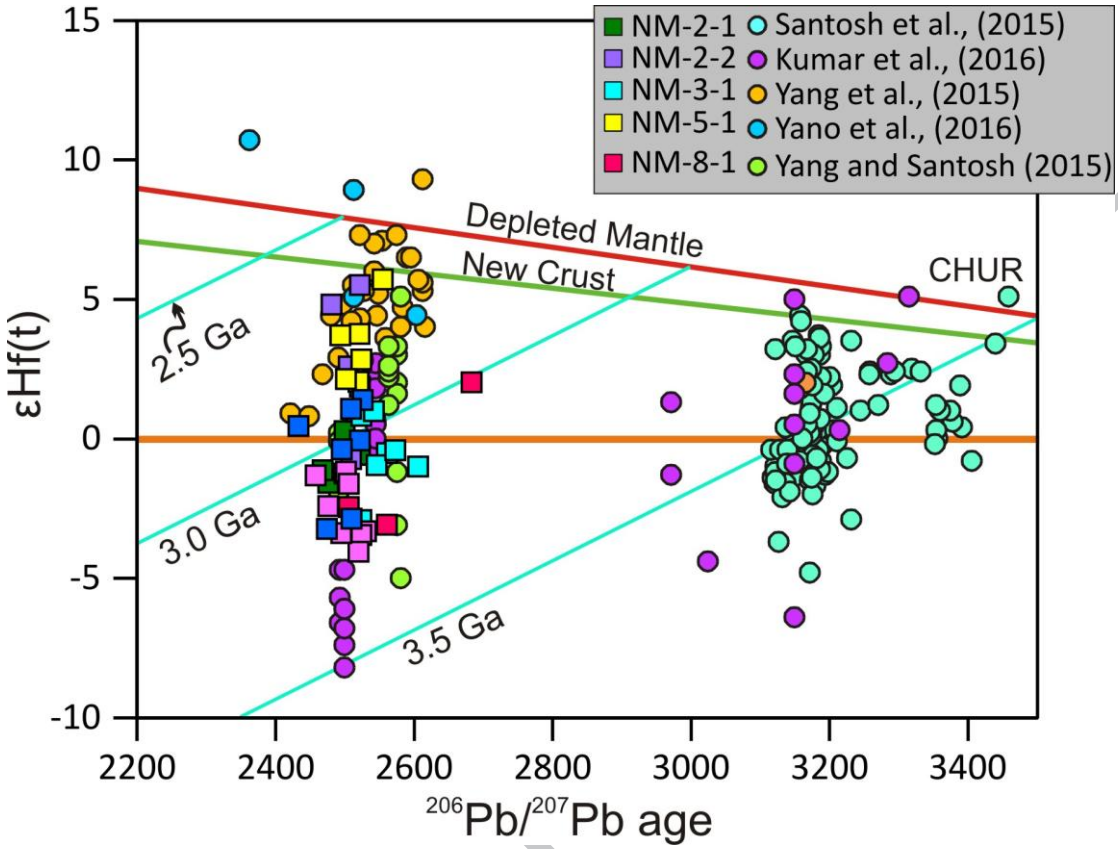

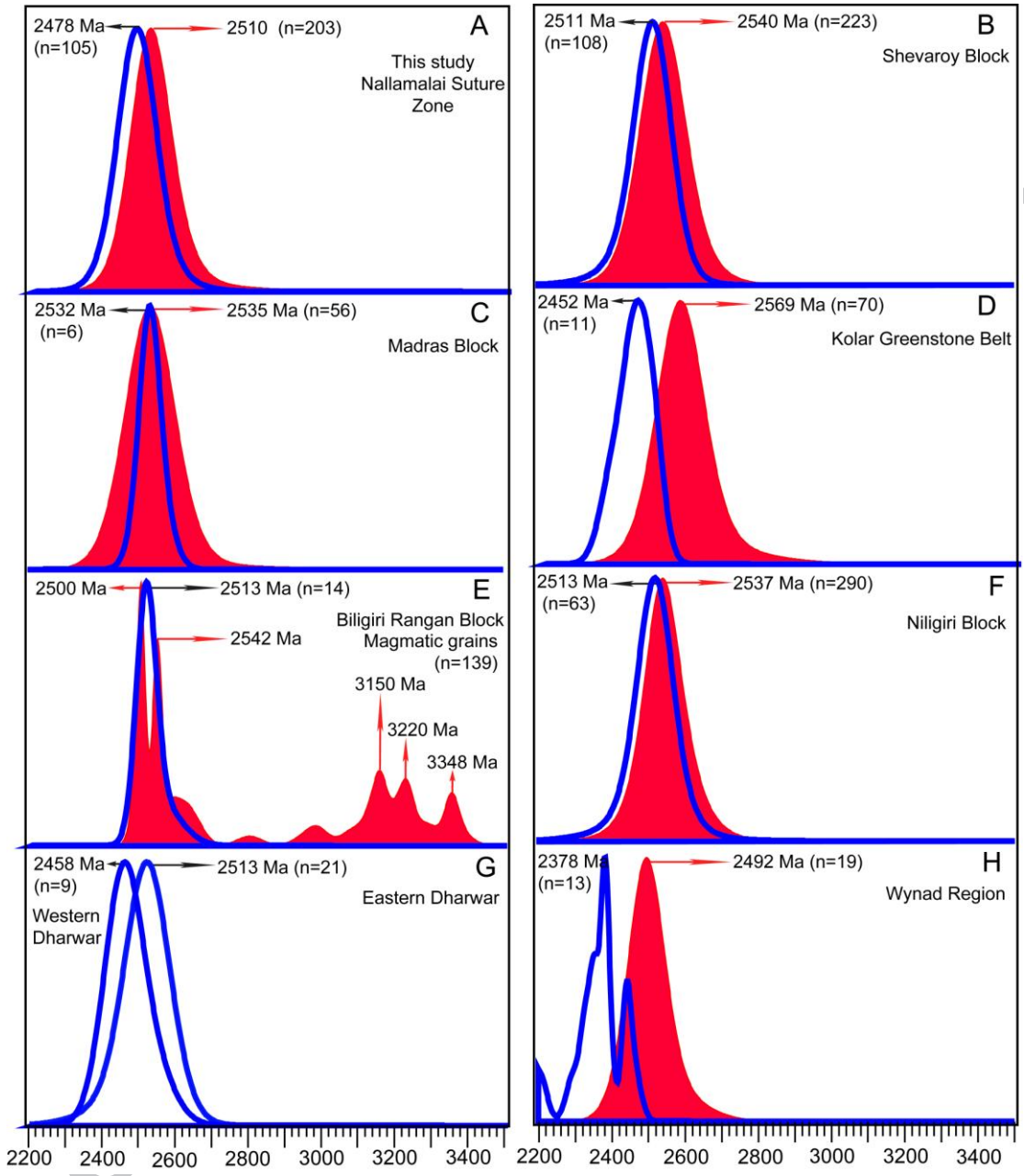

Table 1 Sample numbers, rock types, localities, GPS reading of samples from Nallamalai Suture Zone.

Serial No.	Sample NO.	Rock type	Location Name	Coordinates	Analysis			Altitude (m)
					T	G	D	
1	NM-2-1	Charnockite	Periyampatti	12º14′44.21″, 78º10′50.03″	●	●	●	476
2	NM-2-2	Diorite			●	●	●	
3	NM-3-1	Granodiorite	Kattuseegalahalli, North of Karimangalam	12º19′52.14″, 78º12′44.54″	●	●	●	493
4	NM-4-1	Granite	Sellampatti, Appukottai	12º20′40.11″, 78º18′12.45″	●	●		447
5	NM-5-1	Amphibolite	Piranjiunur, S-E of Pochamapalli	12º18′44.13″, 78º22′59.03″	●	●	●	430
6	NM-5-2	Amphibolite				●		
7	NM-5-3	Amphibolite				●		
8	NM-8-1	Meta-monzogranite	Matrapalli	12º25′30.60″, 78º36′08.48″	●	●	●	374
9	NM-8-2	Amphibolite			●	●		
10	NM-11-1	Grt-charnockite	Govindapuram	12º18′05.73″, 78º35′11.79″	●	●		356
11	NM-12-1	Hbl gneiss	Singapalayam	12º28′34.07″, 78º39′27.25″	●	●		423
12	NM-13-1	Charnockite	Anandhavadi	12º15′25.23″, 78º39′48.32″	●	●		352
13	NM-14-1	BIF	Arasankanni	12º15′52.95″, 78º40′50.03″	●	●	●	346
14	NM-14-2	BIF			●	●	●	
15	NM-14-3	BMQ			●	●	●	
16	NM-14-4	BMQ			●	●		
17	NM-15-1	BIF	Thandampattu	12º15′55.36″, 78º41′15.19″	●	●		339
18	NM-16-1	Granitic pegmatite	Melvanakkambadi	12º14′46.91″, 78º43′50.07″	●		●	303
19	NM-16-2	Grt-charnockite			●	●	●	
20	NM-17-1	Grt-Bt gneiss	Naradapattu	12º13′11.74″, 78º44′22.53″	●	●		320

Note: T—Thin section; G—Geochemistry; D—Dating.

Research Highlights

- Neoarchean subduction-related magmatism during ocean-continent convergence
- Tholeiitic to calc-alkaline parental melts for mafic-intermediate-felsic suite
- BIFs derived by chemical precipitation in oceanic realm and deposited in arc related off-shelf environment
- Magmatic and tectonic attributes suggest that the NLSZ is an oceanic suture
- Multiple subduction and amalgamation of microblocks during Archean – Paleoproterozoic transition.